Chemical Engineering Journal 525 (2025) 169863

Contents lists available at ScienceDirect

Chemical Engineering Journal

journal homepage: www.elsevier.com/locate/cej

Towards improved activity and stability in RWGS reaction: Dispersed copper in mesoporous alumina matrix as a strategy for enhanced performance

Simi Saju [a], Sivaraj Rajendran [a], Ulviye Öztas [b], Sergio Carrasco Ruiz [c], Tomas Ramirez Reina [c], Biplab Ghosh [d], Sreeprasanth Pulinthanathu Sree [e], Raghavendra Meena [f], Guanna Li [f], Luis F. Bobadilla [c], Chathakudath P. Vinod [g], Thomas Mathew [a,b,*], N. Raveendran Shiju [b,*]

[a] Department of Chemistry, St. John's College (Affil. University of Kerala), Anchal, Kerala, 691306, India
[b] Catalysis Engineering Group, Van 't Hoff Institute for Molecular Sciences, University of Amsterdam, Science Park 904, 1090 GD Amsterdam, The Netherlands
[c] Inorganic Chemistry Department and Materials Science Institute, University of Seville-CSIC, 41092, Sevilla, Spain
[d] Beamline Development & Application Section, Bhabha Atomic Research Center, Mumbai, 400085, India
[e] Center for Surface Chemistry and Catalysis: Characterization and Application Team and Department of Materials Engineering, University of Leuven, Leuven, 3001, Belgium
[f] Biobased Chemistry and Technology, Wageningen University & Research, Bornse Weilanden 9, Wageningen, 6708WG, The Netherlands
[g] Catalysis and Inorganic Chemistry Division, CSIR-National Chemical Laboratory (NCL), Pune, India

A B S T R A C T

The development of highly performing Cu-based catalysts with high dispersion of Cu species in nanocrystalline form on a suitable oxide support is significant in reverse water gas shift (RWGS) reaction. We report a simple and robust one-pot sol-gel synthesis of mesoporous $Al_{10-x}Cu_xO_y$ (mγ-$Al_{10-x}Cu_x$-SG) catalysts with Cu species in a highly dispersed nanocrystalline form in the γ-Al_2O_3 matrix and its high catalytic performance in RWGS reaction. The lack of long range structural order of copper species in mγ-$Al_{10-x}Cu_x$-SG catalysts evidenced from Cu—K edge extended X-ray absorption fine structure (EXAFS) studies illustrates the fine distribution of copper species in mesoporous γ-Al_2O_3 lattice. Activity study revealed that mγ-$Al_{10-x}Cu_x$-SG catalysts showed significantly high CO_2 conversion to CO and excellent catalytic stability compared to γ-$Al_{10-x}Cu_x$-I prepared by conventional impregnation method. Mesoporous Al_9Cu_1 (mγ-Al_9Cu_1) displayed a CO_2 conversion of 45 % at 500 °C, which is about 2.8 times higher activity than conventional γ-Al_9Cu_1-I catalyst with almost same Cu loading as that of mγ-Al_9Cu_1 catalyst. Stability study at 500 °C over a period of 50 h revealed that mγ-$Al_{10-x}Cu_x$-SG catalysts at low Cu loading (mγ-$Al_{9.9}Cu_{0.1}$) showed excellent catalytic stability. The strong copper-alumina interaction in mγ-$Al_{10-x}Cu_x$-SG catalysts with enhanced number of active sites at the copper-alumina interface as evidenced from field emission scanning electron microscope (FESEM), high-resolution transmission electron microscope (HRTEM), H_2–temperature programmed reduction (H_2-TPR), X-ray photoelectron spectroscopy (XPS), electrochemical characterization, and Cu—K edge EXAFS analysis enhances the activity and stability of the catalyst. Density functional theory (DFT) studies and the *Operando* DRIFTS-MS analysis of RWGS over mγ-Al_9Cu_1 catalyst revealed that the mechanism of RWGS reaction to CO formation on mγ-$Al_{10-x}Cu_x$-SG catalysts is preceded through the formation of a hydroxycarbonyl (OCOH) intermediate. The present synthesis strategy provides an opportunity for producing Cu-based catalysts with further enhanced activity and stability in RWGS reaction by suitable modification of the catalyst.

1. Introduction

CO_2 conversion to CO by catalytic hydrogenation via reversible water gas shift (RWGS) reaction is a highly attractive and industrially relevant reaction due to the reason that CO is a potential feedstock upon which many industrial processes like methanol production, Fischer–-Tropsch synthesis, and Monsanto/Cativa acetic acid synthesis relies [1–4]. The production of liquid fuels and chemicals by integrating the RWGS process using atmospheric CO_2 as a sustainable feedstock with well-established processes, such as Fischer–Tropsch (FT) synthesis and methanol synthesis is especially promising if the process can incorporate H_2 from a renewable energy process, which offers a promising solution for solving the environmental issues and energy crisis pertaining to the continuous use of fossil fuels [1–3]. However, the high temperature operating profile of the endothermic RWGS reaction poses a real challenge in developing highly active, CO selective, and thermally stable RWGS catalysts [5,6]. Among various catalysts, Cu-based catalysts are highly attractive in RWGS reaction due to the high CO_2 hydrogenation activity and CO selectivity of copper, and it's cheaper availability compared to noble metals [2,6–8]. However, the difficulty in achieving

* Corresponding authors.
E-mail addresses: thomasmathew@stjohns.ac.in (T. Mathew), n.r.shiju@uva.nl (N.R. Shiju).

https://doi.org/10.1016/j.cej.2025.169863
Received 3 May 2025; Received in revised form 20 September 2025; Accepted 18 October 2025
Available online 21 October 2025

highly dispersed Cu species in nanocrystalline form by conventional catalyst preparation methods, and the catalyst deactivation due to the low thermal stability and sintering of supported copper particles under the harsh reaction conditions are the major drawbacks of Cu-based RWGS catalysts [2,6–9]. Different strategies like use of irreducible and reducible oxide supports and various other substrates such as transition metal carbides, perovskite-type oxides, etc., support modification, stabilization of Cu particles through confinement effect by incorporating Cu particles into the pores of porous structured materials such as zeolites and mesoporous silica, preparation method, alloying with other metals, use of basic metal and electronic promoters, by preparing in stable crystalline phases such as spinel oxide and layered double hydroxide forms, etc. have been adopted in the literature to develop Cu-based RWGS catalysts with improved activity and stability [8–20].

The catalyst support has a crucial role in the catalytic activity and stability of Cu-based catalysts in RWGS reaction by dispersing and modifying the chemical nature of the active component [13–20]. Hence the role of catalyst support and its modification would appear to offer the most chances of improving the stability while maintaining high activity and CO selectivity. Among all supports, alumina is more attractive and widely used support in RWGS reaction and several commercial reactions such as CO_2 hydrogenation to CH_3OH and CH_4 due to its interesting physico-chemical characteristics, high surface area, cheap and easy availability [11,17,21]. However, CO_2 adsorption and its activation are generally regarded to be moderate on Al_2O_3 [6,11]. Further, the RWGS reaction over conventionally prepared Al_2O_3 supported Cu catalysts shows poor activity at low Cu loading due to insufficient active sites whereas at high Cu loading (>5 %) the Cu-Al_2O_3 interaction is weak and it shows fast decay of catalytic activity due to severe agglomeration of Cu nanoparticles at high temperature [11,17,20].

Mesoporous alumina and mesoporous alumina supported metal oxides with tunable pore sizes and narrow pore size distribution have given significant research importance in chemical and material field due to its interesting physico-chemical properties and potential applications in adsorption and catalysis [22,23]. Compared to conventional alumina, mesoporous alumina has unique advantages in heterogeneous catalytic reactions due to high surface area and thermal stability, highly exposed and increased number of active sites, easy diffusion and migration of reactants and products in and out of the catalyst surface [23]. Therefore, the drawbacks associated with conventional Cu/γ-Al_2O_3 could be prevented if catalytically active Cu ion species are introduced into a mesoporous alumina framework. Mesoporous Cu/γ-Al_2O_3 can offer more active sites for RWGS reaction by accommodating the active copper species in sufficient number and effectively enhancing the dispersion of active copper species in nanocrystalline form, and also can withstand the reaction conditions by confining the active Cu particles inside the mesopores and significantly improving the copper-alumina interaction [24]. Moreover, γ-Al_2O_3 in mesoporous form improve the activation and hydrogenation of CO_2 molecules by providing more Lewis acid and Bronsted acid centers and allow the re-dispersion of active copper component during the reaction, thus improving the activity and stability of the catalyst.

Herein, we report the synthesis of CuO nanoparticles integrated in a mesoporous γ-Al_2O_3 having the general composition of $Al_{10-x}Cu_xO_y$ (where x = 0.1, 0.5, 1 and 1.5) via a facile one-pot sol-gel route and demonstrate its high CO_2 conversion to CO and enhanced stability in RWGS reaction. Unlike the conventional preparation methods such as impregnation, the sol-gel method adopted here overcomes the difficulty in achieving effective dispersion of Cu nanoparticles at higher Cu loading in γ-Al_2O_3 lattice to provide a greater number of active sites for high activity in RWGS reaction. Detailed structural characterization of mesoporous $Al_{10-x}Cu_xO_y$ (henceforth abbreviated as mγ-$Al_{10-x}Cu_x$-SG) catalysts revealed that CuO_x species are in a highly dispersed nanocrystalline state through strong Cu-Al_2O_3 interaction in mγ-$Al_{10-x}Cu_x$-SG, which enhances the catalyst stability and provides an optimum concentration of surface active sites for CO_2 and H_2 adsorption and their activation in accelerating the rate of reaction. Moreover, the mesoporosity of the material enhances the diffusion rate of reactants and products on the catalyst surface and also offers a spatial confinement effect to the active CuO_x species, which could enhance the overall activity and catalyst stability by retarding the agglomeration of Cu particles during the course of the reaction. The synthesis approach described in this work is very simple and robust in the sense that we use readily available structure directing agents ethylenediaminetetraacetic acid (EDTA) and ethylenediamine (ED) rather than any expensive surfactants to fabricate $Al_{10-x}Cu_xO_y$ in a mesoporous form and it is a potential strategy to address the issues related to conventional and other Cu-based catalysts in the RWGS reaction.

2. Experimental section

2.1. Catalyst synthesis

Aluminium (III) nitrate nonahydrate ($Al(NO_3)_3{\cdot}9H_2O$, Sigma-Aldrich), copper (II) nitrate trihydrate ($Cu(NO_3)_2{\cdot}3H_2O$, SRL), ethylenediaminetetraacetic acid (EDTA, Loba Chemie), ethylenediamine (ED, Merck), and γ-Al_2O_3 (Aldrich, surface area 205 m^2/g) were used as such without any further purification. Mesoporous Cu^{2+} ion incorporated γ-Al_2O_3 (mγ-$Al_{10-x}Cu_x$-SG) having the general formula $Al_{10-x}Cu_xO_y$ (where x = 0.1, 0.5, 1 and 1.5) was prepared by a one-pot sol-gel synthesis technique combining EDTA and ED in aqueous media by a similar procedure as described earlier in the literature [23,25]. Initially, an aqueous solution of metal ion precursors of 0.5 M concentration was prepared by using $Al(NO_3)_3{\cdot}9H_2O$: EDTA: ED in 1:1:3 M ratio, and $Cu(NO_3)_2{\cdot}3H_2O$: EDTA: ED in 1:1:2 M ratio, for Al^{3+} and Cu^{2+}, respectively. For the preparation of Al^{3+} precursor solution, 0.15 mol of ED was added to an aqueous suspension of EDTA-water mixture containing 0.05 mol of EDTA with gentle stirring. To the clear solution of the EDTA-ED mixture, 0.05 mol of $Al(NO_3)_3{\cdot}9H_2O$ was added and then heated at 80-90 °C with vigorous stirring till it becomes a clear solution and subsequently made up to 100 mL. The preparation of 0.5 M Cu^{2+} ion solution was accomplished by dissolving 0.05 mol of $Cu(NO_3)_2{\cdot}3H_2O$ in an aqueous solution containing 0.05 mol of EDTA and 0.1 mol of ED and the whole solution was then made up to 100 mL. The Al^{3+} and Cu^{2+} precursor solutions were then mixed in different proportions for preparing mγ-$Al_{9.9}Cu_{0.1}$, mγ-$Al_{9.5}Cu_{0.5}$, mγ-Al_9Cu_1 and mγ-$Al_{8.5}Cu_{1.5}$ catalysts. As an example, for the preparation of mγ-Al_9Cu_1 catalyst, 27 mL of 0.5 M Al^{3+}-solution, and 3 mL of 0.5 M Cu^{2+}-solution were thoroughly mixed in a 250 mL beaker and stirred for 5 min. The mixed solution on heating at 60 °C for 24–36 h in an air oven resulted in a bluish gel. The gel when heated at 200 °C for 4 h at a heating rate of 2 °C/min was transformed into a voluminous carbonaceous material, which was powdered and finally calcined at 500 °C for 4 h at a heating rate of 2 °C/min. The sol-gel synthesis sequences involved in the mγ-$Al_{10-x}Cu_x$-SG formation is presented in Scheme 1. For mesoporous γ-Al_2O_3 (mγ-Al_2O_3) synthesis, Al precursor solution (0.5 M, 11 mL) alone was used and followed the same synthesis steps as described in Scheme 1. A CuO/Al_2O_3 catalyst with an almost same amount of Cu content as that of mγ-Al_9Cu_1 (10 mol% Cu based on Al and Cu content or 12.17 wt% of Cu based on the weight of Cu in the reduced state and Al_2O_3 weight) was also synthesized by a conventional wet impregnation method, and it was used as reference material (designated as γ-Al_9Cu_1-I) for comparison. For the preparation of γ-Al_9Cu_1-I, about 4.59 g of γ-Al_2O_3 was added to 40 mL aqueous solution containing 2.42 g of $Cu(NO_3)_2{\cdot}3H_2O$. The resulting mixture was sonicated for 30 min and the suspension thus obtained was dried overnight at 120 °C. The dried solid powder was then grinded well and eventually calcined at 500 °C for 4 h at a heating rate of 2 °C/min.

2.2. Physico-chemical characterization

X-ray diffraction (XRD) patterns were recorded on a Panalytical Aeris

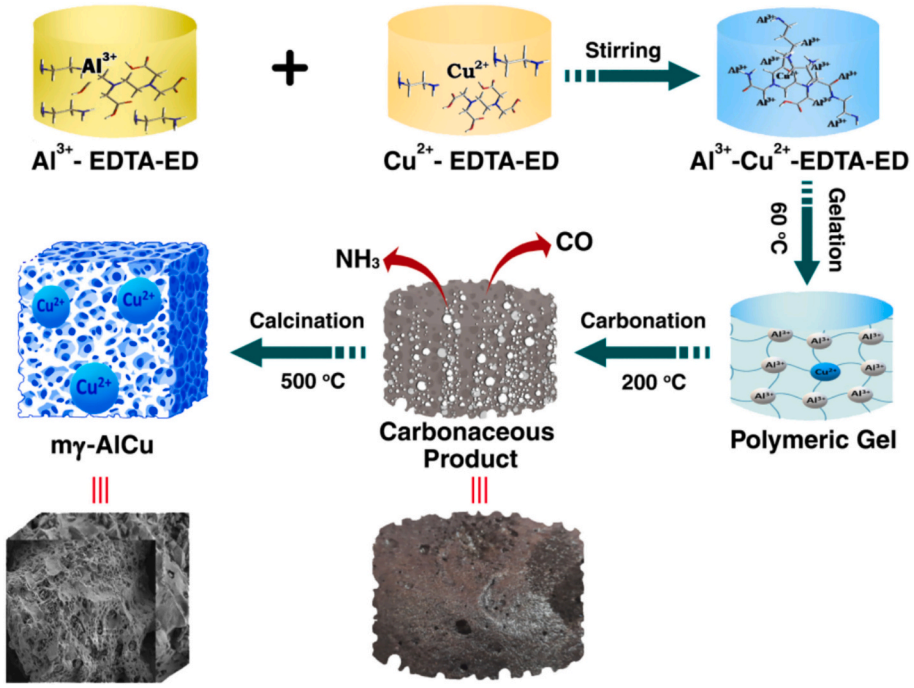

Scheme 1. Schematic illustration of the sequential processes involved in the synthesis of mesoporous $Al_{10-x}Cu_xO_y$ (mγ-$Al_{10-x}Cu_x$-SG) catalysts.

X-ray diffractometer using Cu Kα radiation (λ =1.5406 Å) with a Ni filter to identify the phase characteristics of the material. Each sample was scanned at a rate of 5^0/min, in the 2θ range of 10 to 80^o. The N_2 adsorption analysis was performed at liquid N_2 temperature (77 K) on a Quantachrome autosorb automated gas sorption system (NOVA 1200) and/or Micrometrics TriStar II 3020 apparatus (Norcross, GA, USA) to study the textural properties of the catalysts. The catalysts were pre-heated at 250 °C for 2 h under vacuum before the adsorption-desorption analysis. Specific surface area was calculated from the adsorption branch of the isotherm using Brunauer–Emmett–Teller (BET) equation. The average pore size and pore volume were calculated by the Barret–Joyner–Halenda (BJH) method. High resolution scanning electron microscopic (HRSEM) images and energy dispersive X-ray (EDX) measurements were performed on a Nova Nano SEM450 microscope (FEI, Hillsboro, OR). Field emission scanning electron microscopic (FESEM) and energy dispersive X-ray (EDX) measurements were carried out on a Carl Zeiss-Sigma 300 microscope. Transmission electron microscopic (TEM) and high-resolution TEM (HRTEM) images and energy dispersive X-ray (EDX) measurements were obtained using the JEOL/JEM 2100 instrument at an accelerating voltage of 200 kV. The HRTEM and selected area electron diffraction (SAED) pattern of selected samples were measured on a JEOL/JEM 2100 electron microscope at 200 kV with LaB_6 as the electron gun. X-ray photoelectron spectroscopy (XPS) analysis was carried out on a Thermo Scientific photoelectron spectrometer using a monochromatic Al K*α* anode (1486.6 eV) as an X-ray source. The binding energy (BE) correction was applied for each element by taking C 1 s peak (284.6 eV) as reference. For quantification, the peak intensities of each element was estimated and employed along with photoionization cross section factors [26]. The H_2_temperature programmed reduction (H_2-TPR) analysis was performed in a U-shaped quartz reactor. Before TPR measurement, each sample was treated at 150 °C for 1 h in a flow of Ar. Subsequently, TPR analysis was carried out by heating the sample from room temperature to 950 °C at a heating rate of 10 °C/min while 5 % H_2/Ar reactive gas stream was passed through the catalyst. A thermal conductivity detector (TCD) was used for measuring the hydrogen consumption. A standard sample of CuO (Sigma-Aldrich 99.99 %) was used as reference for calibration.

The X-ray absorption spectroscopy (XAS) measurements including both Cu K-edge X-ray absorption near edge structure (XANES) and Cu K-edge extended X-ray absorption fine structure (EXAFS) analyses were performed using the energy scanning EXAFS beamline (BL-09) facility installed at Indus-2 (2.5 GeV and 300 mA) at the Raja Ramanna Centre for Advanced Technology (RRCAT), Indore, India. The XAS analysis of all the samples was performed in transmission mode. The energy range of the beam line is 4 to 25 keV [27]. The beamline optics mainly consists of a Si (111) Double Crystal Monochromator (DCM) with continuous-scan mode. Data processing and analysis of XANES and EXAFS was carried out using different modules of the Demeter software package [28]. Hephaestus module was used to obtain energy edge positions and Athena module was employed for data processing, including background removal, normalization, pre-edge and post edge correction and Fourier transform techniques. Artemis module of same software package was used for EXAFS fitting (modeling) using the scattering paths generated from the crystallographic data of CuO (COD ID 1011148) [29]. The EXAFS fitting details are provided in the supporting information.

2.3. Catalyst activity evaluation

The catalytic performance of the mγ-$Al_{10-x}Cu_x$-SG and γ-$Al_{10-x}Cu_x$-I catalysts were recorded in an automated six-flow parallel reactor system, consisting of six quartz tube down flow reactors with an inner diameter of 7 mm as previously reported [30]. About100 mg of catalyst was used for each measurement, and it was kept on the porous structured quartz support in the middle of the reactor. The catalysts were pre-heated at 400 °C in a flow of N_2 before the activity measurements. The catalytic evaluation was carried out at a H_2:CO_2 ratio of 4:1 under atmospheric pressure. The flow rates of CO_2, H_2, and Ar were maintained at 10, 40, and 50 mL/min, respectively by means of mass flow controllers. The temperature screening of the catalysts was performed between 300 and 600 °C by introducing the above gas mixture with H_2/CO_2 ratio of 4 into the reactor system at a constant weight hourly space velocity (WHSV) of 12,000 mL g^{-1} h^{-1}. The duration of each temperature screening test was 1 h. The stability tests of the catalysts were performed at 500 °C at the same space velocity of 12,000 mL using the above gas mixture with H_2/CO_2 at a mole ratio of 4. All the catalysts

were reduced in a flow of 10 % H_2/N_2 at 400 °C for 30 min before the reaction. The CO_2 conversion and CO selectivity calculated was within the error limit of ±5 % for all the experiments. The reactants and products were analyzed using an online gas chromatograph, equipped with both thermal conductivity and flame ionization detectors. The CO_2 conversion and CO selectivity was calculated using the Eqs. (1) and (2) to evaluate the performances of the catalysts.

$$CO_2 \text{ conversion } (\%) = \frac{[CO_2]_{in} - [CO_2]_{out}}{[CO_2]_{in}} \times 100 \quad (1)$$

$$CO \text{ selectivity } (\%) = \frac{[CO]_{out}}{[CO_2]_{in} - [CO_2]_{out}} \times 100 \quad (2)$$

2.4. Density functional theory (DFT) calculation details

All the density functional theory (DFT) calculations were performed with the Vienna ab initio simulation package (VASP.6.2.1) [31,32]. The generalized gradient approximation (GGA) with PBE exchange and correlation functional was used to account for the exchange-correlation energy [33]. The *electron–ion* interactions were described using the projected augmented wave (PAW) method and the plane-wave (PW) basis set [31,32]. The kinetic energy cut-off of the plane wave basis set was set to 520 eV. The convergence criterion for energy calculation and structure relaxation was set to a self-consistent field threshold of 10^{-5} eV, and a maximum force threshold of 0.05 eV/Å. The bulk structures of Cu (mp-30) and γ-Al_2O_3 (mp-1143) were taken from the materials project database and were fully relaxed. Γ-centered k-meshes of the size of 6 × 6 × 6 and 5 × 5 × 2 were used for sampling the Brillouin zone in the case of bulk of Cu and γ-Al_2O_3, respectively. After relaxing the atoms in the unit cell, we created a supercell of the sizes of 4 × 3 × 1 and 2 × 2 × 1, for Cu (111) and γ-Al_2O_3 (110), respectively. The stable terminations, based on previous works, were cleaved for Cu (111) [34] and γ-Al_2O_3(110) [35,36]. The bottom four and six atomic layers of Cu (111) and γ-Al_2O_3 (110) supercells, respectively, were fixed to reduce the computational cost of the calculations and to mimic the bulk. Γ-centered k-mesh of the size of 2 × 2 × 1 was used for sampling the Brillouin zone for both surface slab models. Gaussian-type smearing with a width of 0.05 eV was applied for the electronic energy density of states. For identifying the transition states, the climbing-image nudged elastic band (CI-NEB) method was used, and frequency analysis was performed to confirm that there was only one imaginary frequency along the reaction coordinate. For CI-NEB calculations, the maximum force threshold of 0.10 eV/Å was implemented. Vacuum distances of 15 Å and 12 Å were introduced to the slab models of Cu (111) and γ-Al_2O_3 (110), respectively, in the z-direction to minimize interaction with the periodic images. Dipole corrections were applied in the vacuum (z) direction. The van der Waals interactions were described by the DFT-D3BJ method developed by Grimme et al. [37,38]

The adsorption energies (E_{ads}), reaction energies (ΔE), and activation barriers (E_a) were calculated as follows:

$$E_{ads} = E_{slab+reactant} - E_{slab} - E_{reactant} \quad (3)$$

$$\Delta E = E_{product} - E_{reactant} \quad (4)$$

$$E_a = E_{transition\ state} - E_{reactant} \quad (5)$$

Here, $E_{slab+reactant}$ is the total energy of the slab with a reactant adsorbed on it, E_{slab} is the total energy of the clean slab, $E_{reactant}$ and $E_{product}$ are the total energies of the reactant and product of each elementary reaction step, and $E_{transition\ state}$ is the total energy of the transition state (TS). The thermodynamic corrections to Gibbs free energies have been applied to all the intermediates and TS based on harmonic frequency calculation, as implemented in VASP, and VASPKIT [39] was used for data post-processing with the reaction temperature of 350 °C and pressure of 1 atm.

3. Results and discussion

3.1. Synthesis aspects and characterization (XRD, FESEM, TEM, N_2 adsorption, and TPR) of mγ-$Al_{10-x}Cu_x$-SG catalysts

The Al^{3+} and Cu^{2+}cations in aqueous solution undergo chelation with the structure directing chelating reagents EDTA and ED [23]. The EDTA with four carboxyl groups and ED with two amino groups are strongly coordinating and they have the advantage of holding both Al^{3+} and Cu^{2+} ions in the organic gel network through chelation. The distinct advantage of these chelating ligands is that the formation of stable metal hydroxy species through extensive hydrolysis and condensation reactions and/or precipitation reactions is prevented during the initial sol formation. The sol containing EDTA-ED combination, and the metal cations coordinated to the structure directing agents on controlled heating at 60 °C undergo cross-linking by extensive condensation reaction between the free –COOH group in EDTA and an amine group in ED to form a transparent polyamide gel network accommodated with Al^{3+} and Cu^{2+} ions. The structure directing agents play multiple roles in this sol-gel process, such as stabilizing the metal ions through chelation, speeding up the condensation and gelation process, and also functioning as fuel during the heat treatment. The polymeric gel on further heating at 200 °C leads to extensive condensation and cross-linking to form a voluminous black colored carbonaceous product with the release of gaseous products such as NH_3, hydrocarbons, CO, and H_2O. The black-colored product on subsequent calcinations at 500 °C in air burns out the carbonaceous species to form mγ-$Al_{10-x}Cu_x$-SG nanocomposites. The advantageous aspect of adopting such a sol-gel process by employing a combination of chelating agents is to trap Al^{3+} and Cu^{2+} ions in the polymer gel and to achieve highly dispersed metal ions all throughout the polymeric framework, whereas in conventional sol-gel method the particles also become the part of the gel structure [40]. This cooperative organization of organic and inorganic species through different kinds of physical and chemical interactions allows fine distribution of Cu^{2+} ions at the nanoscale level in the mesoporous γ-Al_2O_3 network. This synthesis strategy is suitable for producing highly homogeneous mesoporous Cu-based γ-Al_2O_3 oxides at reduced temperatures.

The XRD patterns of pure mγ-Al_2O_3 and mγ-$Al_{10-x}Cu_x$-SG catalysts prepared by sol-gel method displayed in Fig. 1 exhibit broad diffraction peaks approximately at 2θ = 18.8°, 37.8°, 45.5°, 66.5°, corresponding to (111), (311), (400), (440) reflections of γ-Al_2O_3 (JCPDS 10–0425 & JCPDS 29–0063). However, sharp diffraction peaks characteristic of bulk CuO (JCPDS No. 48–1548) is the dominant phase in the case of conventionally prepared γ-Al_9Cu_1-I catalyst (Fig. 1, F). The broad diffraction features and the absence of diffraction peaks of bulk CuO phase in mγ-$Al_{10-x}Cu_x$-SG catalysts indicate that the particle size of copper species is very small, and copper species are highly dispersed in the γ-Al_2O_3 lattice. However, compared to pure γ-Al_2O_3, slight shift in the 2θ values and minor changes in the peak intensities in the XRD pattern of mγ-$Al_{10-x}Cu_x$-SG is attributed to the possible doping of Cu into γ-Al_2O_3 lattice.

The textural parameters, such as the BET surface area (S_{BET}), pore size by BJH method (D_{BJH}), and pore volume (V_P) derived from N_2 adsorption analysis of mγ-$Al_{10-x}Cu_x$-SG catalysts are given in Table S1 in the supporting information. The N_2 adsorption–desorption isotherm of all mγ-$Al_{10-x}Cu_x$-SG catalysts displayed type IV isotherm (Fig. 2A) indicating the mesoporous nature of the material. Interestingly, the BJH pore size (D_{BJH}) distribution is in the mesopore range of 3–5 nm (Fig. 2B). The BET surface areas (S_{BET}) of $Al_{9.9}Cu_{0.1}$, $Al_{9.5}Cu_{0.5}$, Al_9Cu_1, and $Al_{8.5}Cu_{1.5}$ were 332, 321, 278, and 269 m^2g^{-1}, respectively. The pore volume (V_P) of these materials is in the range of 0.36–0.40 cm^3g^{-1}. It is worth to note that in comparison with pure mesoporous γ-Al_2O_3 (S_{BET} = 323 m^2g^{-1}, D_{BJH} = 6.1 nm, V_P = 0.49 cm^3g^{-1}) (not shown), there is no large decrease of textural parameters even at higher copper loading. The BET surface area, pore size, and pore volume of the conventionally prepared γ-Al_9Cu_1-I catalyst was 125 m^2g^{-1}, 3.6 nm, and

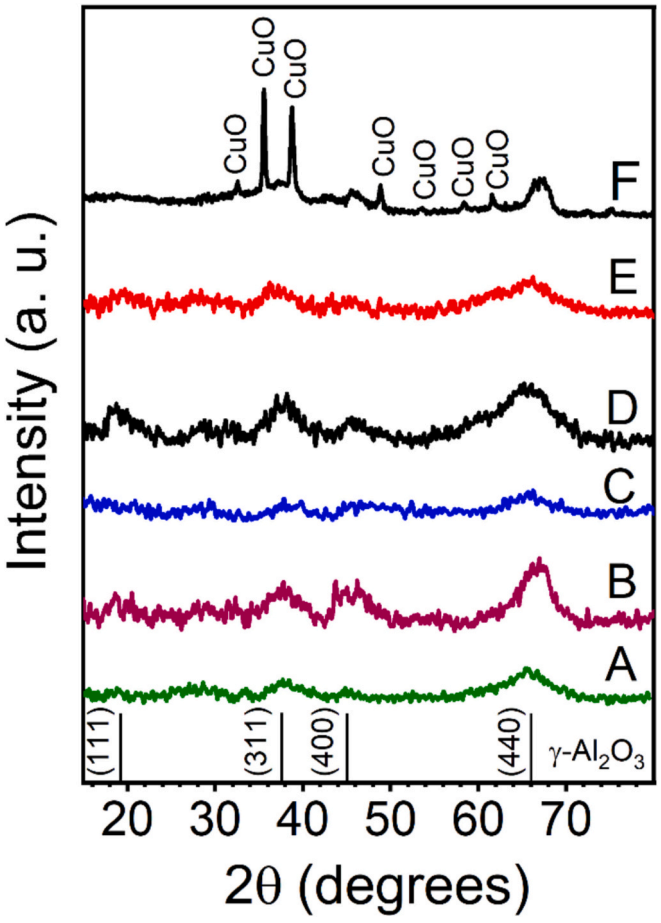

Fig. 1. XRD patterns of mesoporous mγ-$Al_{10-x}Cu_x$-SG catalysts with different copper content prepared by sol-gel process (A: mγ-Al_2O_3, B: mγ-$Al_{9.9}Cu_{0.1}$, C: mγ-$Al_{9.5}Cu_{0.5}$, D: mγ-Al_9Cu_1, E: mγ-$Al_{8.5}Cu_{1.5}$) and γ-Al_9Cu_1-I prepared by conventional impregnation method (F: γ-Al_9Cu_1-I). Note that the XRD intensity of γ-Al_9Cu_1-I was divided by a factor of 5 for a better visualization of the XRD peaks of mγ-$Al_{10-x}Cu_x$-SG catalysts in the same frame.

0.17 cm^3g^{-1}, respectively. This underscores that the present synthesis strategy is capable of accommodating more amount of Cu species with high dispersion in the γ-Al_2O_3 lattice rather than forming any agglomerated Cu species as distinct bulk phase and this result is in line with the observations made from XRD.

The SEM and FESEM analyses of mγ-$Al_{10-x}Cu_x$-SGcatalysts were performed to investigate their surface morphology and the images of a representative composition of mγ-Al_9Cu are displayed in Fig. 3A-C. The SEM (Fig. 3A) and FESEM images (Fig. 3B-C) demonstrate the mγ-$Al_{10-x}Cu_x$-SG catalysts are porous in nature comprised of mesopores and macropores, and the alumina particles are irregular in shape with rough surface. Such a structure with surface roughness and the presence of mesopores and macropores are beneficial for adsorption, easy diffusion of surface reaction species and to minimize the pressure drop issues that may occur during reaction [23]. The SEM and FESEM EDX analysis were performed to confirm the elemental composition and to understand the homogeneity and dispersion of Cu in mγ-Al_9Cu_1, and the results for mγ-Al_9Cu_1 is provided in Fig. 3C-G. The EDS chemical mapping at different spots in the SEM and FESEM images confirmed that the elemental composition is very close to the theoretical value (within the maximum error limit of ±3.2 %) and the copper species are well distributed in the alumina lattice, indicating the good chemical homogeneity of the catalyst (Fig. S1 in the supporting information). A typical SEM EDX pattern is shown in Fig. 3D. The FESEM EDX analysis and elemental mapping images of O, Al and Cu elements (Fig. 3E-G) further indicated fine distribution of copper species all over the alumina surface, illustrating that homogenous hybridization of CuO species and alumina and hence an excellent interface interaction exists between copper and alumina in mγ-$Al_{10-x}Cu_x$-SG catalysts.

TEM and HRTEM images of representative samples of mγ-$Al_{10-x}Cu_x$-SG catalysts provided in Fig. 4A (mγ-$Al_{9.9}Cu_{0.1}$) and Fig. 4B&D (mγ-Al_9Cu_1) demonstrate that the material is comprised of particles in the nano-regime with particle size less than 10 nm. It is also evidenced that the particles are interconnected to form a disordered mesoporous structure. There is hardly any variation in the morphological features and particle size between different compositions. This illustrates that the present preparation method allows higher loading of copper oxide species in alumina without altering the morphology and microstructural characteristics of Al_2O_3. This is likely due to the formation of highly dispersed Cu^{2+}-O-Al^{3+}species in the mγ-$Al_{10-x}Cu_x$-SG catalysts. Irrespective of the copper loading the uniform contrast observed in TEM images and no evidence of segregation of copper particles as separate entity indicates that the material is homogeneous, and the copper species are diffusely dispersed throughout the alumina. The SAED pattern of mγ-Al_9Cu_1 in Fig. 4C displayed broad circular rings characteristic of γ-Al_2O_3 phase with weak electron diffraction features, indicating that the CuO species are nanocrystalline and they are finely dispersed in the mγ-Al_2O_3 lattice [23]. The HRTEM analysis (Fig. 4D) shows isolated CuO species having clear lattice fringes with a spacing of 0.24 nm, which is characteristic of the (111) facets of CuO [25,41]. This further confirms that the copper species in mγ-$Al_{10-x}Cu_x$-SG catalysts are nanocrystalline and there is a close contact between alumina and copper species through strong interaction of the isolated Cu^{2+} ions with the γ-Al_2O_3 lattice [17].

It has been reported in the literature that the activity and stability of Cu/Al_2O_3 is largely dependent on the copper-alumina interaction [17]. H_2-TPR analysis performed on mγ-Al_9Cu_1 and the γ-Al_9Cu_1-I reference catalysts (Fig. 5) in the present study provides further evidence on the relatively strong copper-alumina interaction in mγ-$Al_{10-x}Cu_x$-SG catalysts. The reduction pattern of mγ-Al_9Cu_1 and γ-Al_9Cu_1-I catalysts depicted in the H_2-TPR profile in Fig. 5 is different, suggesting that the strengths of copper-alumina interaction in these two catalysts are different. The mγ-Al_9Cu_1 catalyst showed a sharp high intense peak at 236 °C, followed by a very low intense peak at 280 °C and a relatively broad intense high temperature peak at 330 °C. Contrarily, the conventional γ-Al_9Cu_1-I catalyst displayed the reduction peaks at 224 °C as a sharp intense low temperature peak and a relatively broad intense peak centered at 267 °C with a shoulder at 320 °C. The first two peaks can be assigned to the highly dispersed CuO and bulk CuO species, respectively [17,42]. The shoulder peak at 320 °C is likely due to the presence of fine CuO aggregates consisting of smaller particles strongly bound to the γ-Al_2O_3 lattice. With respect to the conventional γ-Al_9Cu_1-I catalyst, the TPR peaks in the H_2-TPR profile of mγ-Al_9Cu_1 catalyst is shifted to higher temperatures, which can be attributed to the relatively strong interaction of the highly dispersed Cu species with the alumina support [17]. It is important to note that when analyzing TPR profiles, not only the oxidation state and the copper loading should be considered, but also the interaction between copper and the support should be taken into account. Copper is in +2 oxidation state in both mγ-Al_9Cu_1 and γ-Al_9Cu_1-I catalysts, which is confirmed by XPS and Cu K-edge XANES analysis as will be seen below. Also, the copper loading is same in both mγ-Al_9Cu_1 and γ-Al_9Cu_1-I catalysts. Therefore, compared to γ-Al_9Cu_1-I catalyst, the relatively lower H_2 consumption on mγ-Al_9Cu_1 in the H_2-TPR profile is a clear indication that copper has a significantly stronger interaction with the alumina lattice in mγ-Al_9Cu_1 than in conventional γ-Al_9Cu_1-I catalyst, as it likely hinders the reducibility of copper species.

3.2. *XPS studies of mγ-$Al_{10-x}Cu_x$-SG catalysts*

XPS of mγ-$Al_{10-x}Cu_x$-SG and γ-Al_9Cu_1-I catalysts were performed to understand the chemical states of Cu, Al and O and the relative

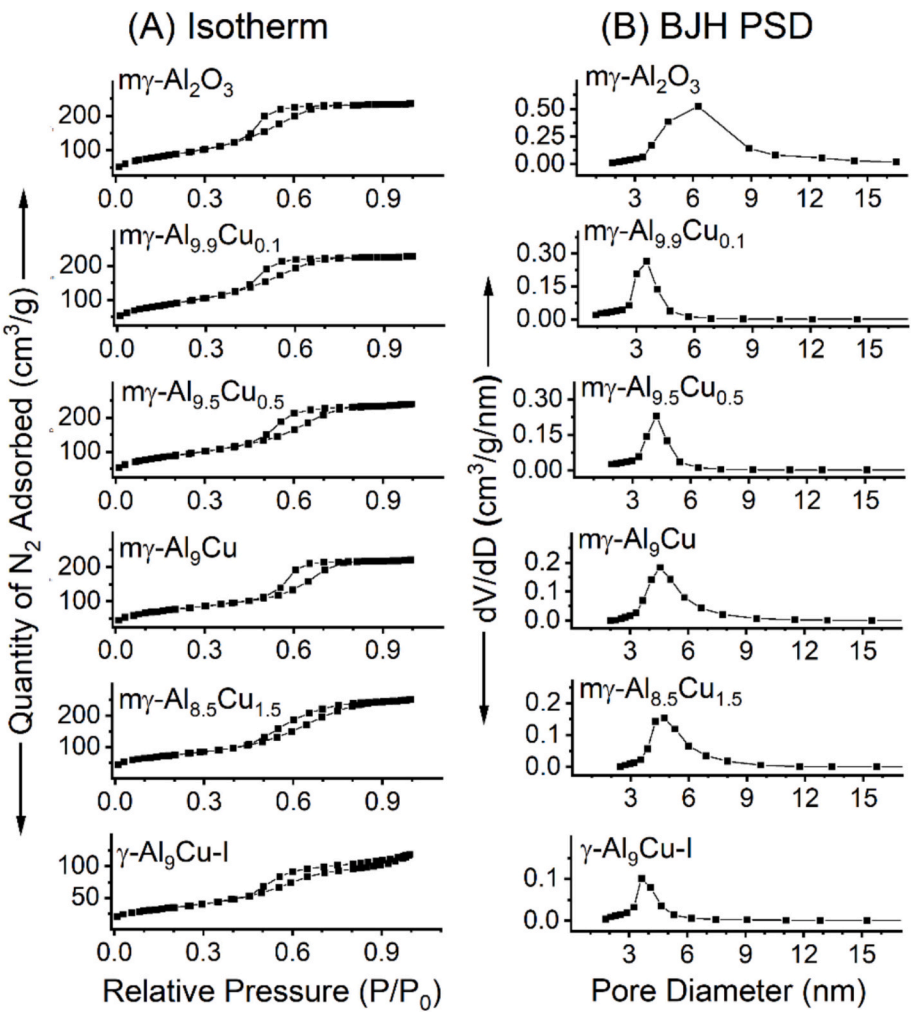

Fig. 2. (A) N_2 adsorption–desorption isotherms, and (B) pore size distribution obtained from N_2 adsorption analysis for mesoporous $Al_{10-x}Cu_xO_y$ (mγ-$Al_{10-x}Cu_x$-SG) catalysts with different copper content prepared by sol-gel process (mγ-Al_2O_3, mγ-$Al_{9.9}Cu_{0.1}$, mγ-$Al_{9.5}Cu_{0.5}$, mγ-Al_9Cu_1, and mγ-$Al_{8.5}Cu_{1.5}$) and conventional γ-Al_9Cu_1-I catalyst prepared by impregnation method.

proportion of Cu and Al on the catalyst surface. XPS parameters derived from various peak components are provided in Table S2 in the supporting information. The Cu 2p XPS spectra of fresh mγ-$Al_{10-x}Cu_x$-SG and γ-Al_9Cu_1-I catalysts shown in Fig. 6A exhibit Cu $2p_{3/2}$ and Cu $2p_{1/2}$ main peaks in the binding energy (BE) ranges 933.6–933.9 eV and 953.5–953.8 eV, respectively with a spin-orbit coupling constant of 19.9 ± 0.1 eV. The BE values and the appearance of an intense satellite feature around 942 eV is a clear indication that the oxidation state of copper is +2 in all samples [17,43]. It can be noticed that the FWHM of Cu 2p3/2 main peak of mγ-$Al_{9.9}Cu_{0.1}$ is 3.07 eV, and it reduces to 2.51–2.56 eV at higher Cu loading. With respect to mγ-$Al_{10-x}Cu_x$-SG catalysts, γ-Al_9Cu_1-I showed a relatively low value of FWHM (2.34 eV), suggesting that the electron density on Cu species is different due to the difference in the strength of metal-support interaction and the chemical environment of copper in the alumina matrix. The BE of the Al 2p XPS spectra of all the catalysts in Table S2 and Fig. S2 (supporting information) fall in the range of 73.5–74.1 eV and is characteristic of Al^{3+} species in copper-alumina mixed oxide system [26].

The O 1 s XPS spectra given in Fig. S3 show a relatively more spectral broadening with a FWHM in the range of 2.93–3.03 eV for mγ-$Al_{10-x}Cu_x$-SG catalysts in comparison with conventional γ-Al_9Cu_1-I catalyst (FWHM of 2.49 eV) (see Table S2 in the supporting information). The O 1 s spectra of all the fresh samples on deconvolution are resolved into two peak components centered at 529.8 and 531.3 eV, which can be assigned to lattice oxygen (O_L) and hydroxyl oxygen (O_H), respectively (Fig. S3) [25,44,45]. With respect to the conventional γ-Al_9Cu_1-I catalyst, the quantity of surface OH species in mγ-$Al_{10-x}Cu_x$-SG catalysts is relatively high. The peak intensity ratio between hydroxyl oxygen (O_H) and lattice oxygen (O_L) estimated for mγ-$Al_{9.9}Cu_{0.1}$, mγ-$Al_{9.5}Cu_{0.5}$, mγ-Al_9Cu_1, mγ-$Al_{8.5}Cu_{1.5}$, and conventional γ-Al_9Cu_1-I catalysts were 0.46, 0.40, 0.30, 0.34, and 0.29, respectively (see Table S3 in the supporting information). The amount of surface OH species on mγ-$Al_{10-x}Cu_x$-SG catalysts are high at low copper content (mγ-$Al_{9.9}Cu_{0.1}$ and mγ-$Al_{9.5}Cu_{0.5}$), however it shows a decreasing trend at higher copper loading (mγ-Al_9Cu_1 and mγ-$Al_{8.5}Cu_{1.5}$). Evidently, the amount of surface hydroxyl groups (-OH) in mγ-$Al_{10-x}Cu_x$-SG catalysts are related to the copper content in the sample to a great extent. At low Cu loading, such as in the case of mγ-$Al_{9.9}Cu_{0.1}$, copper is mainly present as isolated Cu^{2+} ions formed by exchanging with the H atoms of the alumina hydroxyl groups. As the Cu content increases, more and more hydroxyl groups on the alumina surface are consumed and as a result a gradual decrease of hydroxyl group was observed up to mγ-Al_9Cu_1 in the present study. With further increase of Cu loading to mγ-$Al_{8.5}Cu_{1.5}$, the availability of hydroxyl groups for exchange decreases, leading to the formation of bulk copper oxide and the recovery of some hydroxyl groups. Probably this could be the reason for the slight increase of hydroxyl group on mγ-$Al_{8.5}Cu_{1.5}$ with respect to mγ-Al_9Cu_1. Also, the preparation method, interaction between CuO and Al_2O_3, particle size of copper species, surface Cu—Al spinel formation, variation in the heat treatment and calcination processes during the material synthesis etc. are decisive

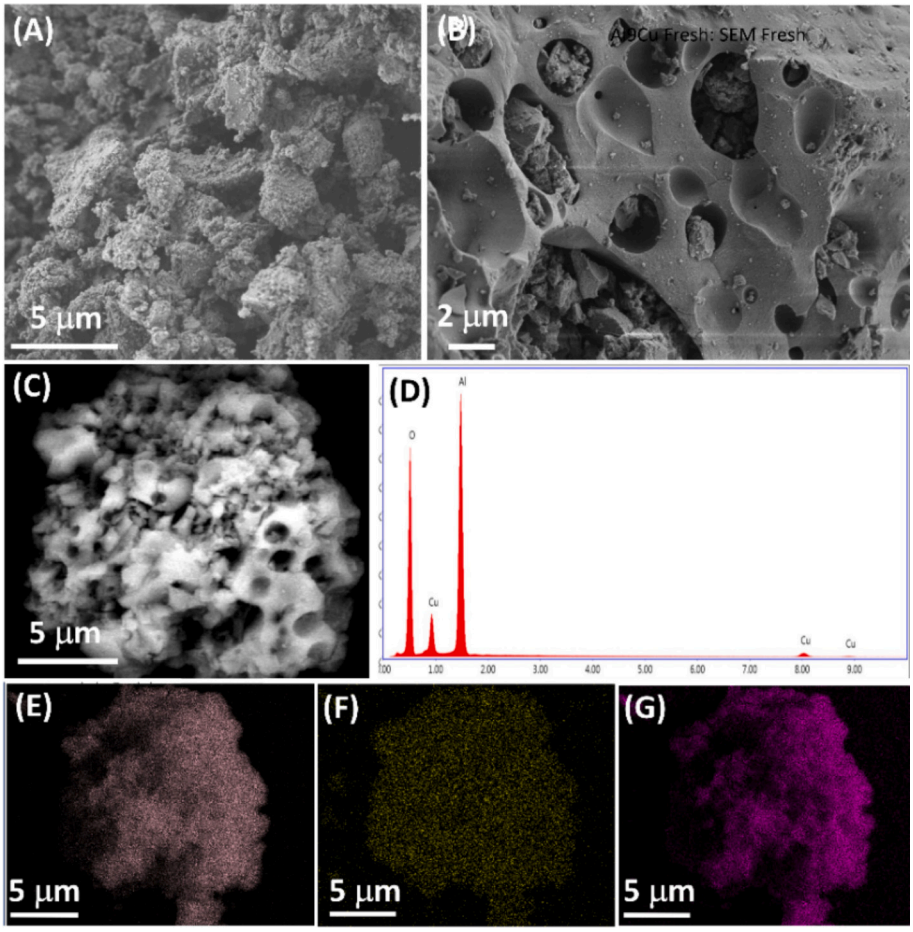

Fig. 3. SEM (A), and FE SEM images of mγ-Al_9Cu_1 (B and C). SEM-EDX spectrum of mγ-Al_9Cu_1 extracted from C (D). The EDS mapping of mγ-Al_9Cu_1: (E) Al, (F) Cu, and (G) O, which reveals uniform distribution of Cu on the alumina surface.

factors that determine the concentration of hydroxyl groups on the catalyst surface.

The valence band (VB) XPS spectra of mγ-$Al_{10-x}Cu_x$-SG and γ-Al_9Cu_1-I catalysts recorded below 15 eV are shown in Fig. 6B. Valence band spectra are essentially comprised of low BE electrons (below 15 eV) occupied by bonding orbitals, and it provide valuable information on the electronic interaction among various elements in the material. The vast difference in the photoionization cross section (σ) values for Cu 3d (0.012 Mb) and O 2p (0.00024 Mb) at $h\nu = 1486.6$ eV and the fact that the first lowest occupied core level of Al^{3+} occurs only at 74 eV benefits in validating VB features in mγ-$Al_{10-x}Cu_x$-SG and γ-Al_9Cu_1-I catalysts [46]. All the catalysts exhibit a main VB feature at around 4–4.5 eV due to Cu 3d bands [25,43]. The intensity of this peak is relatively high for materials at high copper content (mγ-$Al_{8.5}Cu_{1.5}$, mγ-Al_9Cu_1 and γ-Al_9Cu_1-I), but it is reduced for catalysts at low copper loading (mγ-$Al_{9.9}Cu_{0.1}$ and mγ-$Al_{9.5}Cu_{0.5}$). The BE overlap between Cu 3d VB feature at 4–4.5 eV and O 2p feature at 4.5–7.5 eV is due to the strong hybridization of Cu 3d and O 2p orbitals and is characteristic of Cu^{2+}-species [46]. The broad satellite feature at 9–13 eV resulted by the photoionization of $3d^9$ ground state configuration is further evidence that copper exists in +2 oxidation state [25,47]. Nonetheless, this satellite feature is relatively weak in mγ-$Al_{10-x}Cu_x$-SG catalysts compared to γ-Al_9Cu_1-I catalyst, suggesting that the Cu^{2+} species are strongly interacting with Al_2O_3 in mγ-$Al_{10-x}Cu_x$-SG catalysts. Furthermore, the VB spectra also show a shoulder around 2.3 eV, which can be ascribed to the antibonding orbitals of the Cu 3d [46]. This shoulder peak appears to be prominent on Cu rich catalysts (mγ-$Al_{8.5}Cu_{1.5}$, mγ-Al_9Cu_1 and γ-Al_9Cu_1-I) as has been reported for bulk CuO, but it is very weak on mγ-$Al_{10-x}Cu_x$-SG catalysts with low Cu content (mγ-$Al_{9.9}Cu_{0.1}$ and mγ-$Al_{9.5}Cu_{0.5}$).

The surface concentration of Cu and Al were calculated using the relations between the elemental peak intensity, kinetic energy, and photoelectron cross section, as previously reported [43,48]. The peak area of Cu $2p_{3/2}$ and Al 2p were used for the calculation. The Cu/Al surface atomic ratio calculated from XPS for all the catalysts are less than the bulk atomic ratio (Table S2 in the supporting information). The data revealed that the surface concentration of Cu is lowest on mγ-$Al_{9.9}Cu_{0.1}$, and there is a concomitant relation between Cu/Al surface atomic ratio and Cu loading in mγ-$Al_{10-x}Cu_x$-SG catalysts. Among all catalysts in this study, γ-Al_9Cu_1-I showed the highest amount of copper on the surface. The relatively low Cu/Al surface atomic ratio in mγ-$Al_{10-x}Cu_x$-SG catalysts is likely due to the incorporation of more Cu species in the bulk and/or confinement of fine particles of Cu species in the porous structure of the material and its isolation from the surface.

3.3. *XANES and EXAFS studies of mγ-$Al_{10-x}Cu_x$-SG catalysts*

The Cu K-edge XANES and EXAFS analyses were performed in transmission mode for selected catalysts to understand the local structure and electronic states of Cu species in the samples. Cu K-edge XAS absorption spectra is resulted when electronic transition occurs from Cu 1 s state to the unoccupied valence state or into a continuum state [49]. The normalized Cu K-edge XANES spectra of mγ-$Al_{10-x}Cu_x$-SG and γ-Al_9Cu_1-I catalysts are compared with standard sample of CuO in Fig. 7.

The main transition features B and C in the edge portion of the XANES spectrum points to the 1 s → 4p dipole allowed transition. The secondary absorption band feature B is attributed to a shake-down

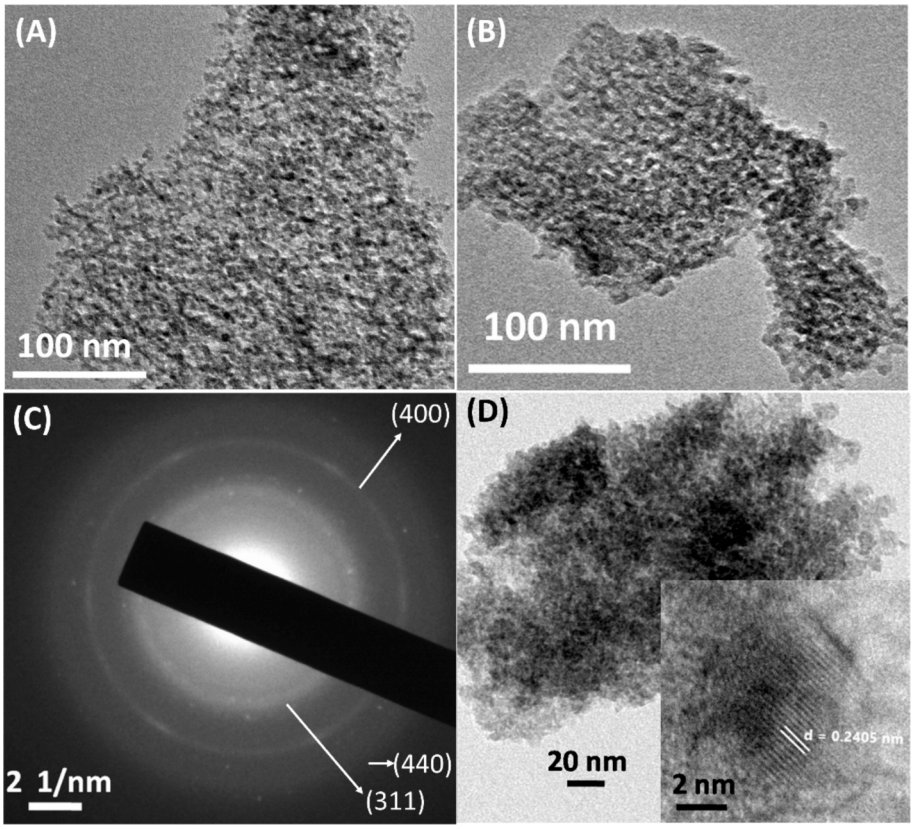

Fig. 4. TEM images of mγ-$Al_{9.9}Cu_{0.1}$ (A) and mγ-Al_9Cu_1 (B). SAED pattern corresponding to the TEM image of mγ-Al_9Cu_1 (C). HRTEM images of mγ-Al_9Cu_1 (D). HRTEM image of mγ-Al_9Cu_1 given in the inset in (D) illustrates the lattice fringes of CuO and the close contact between CuO and alumina lattice.

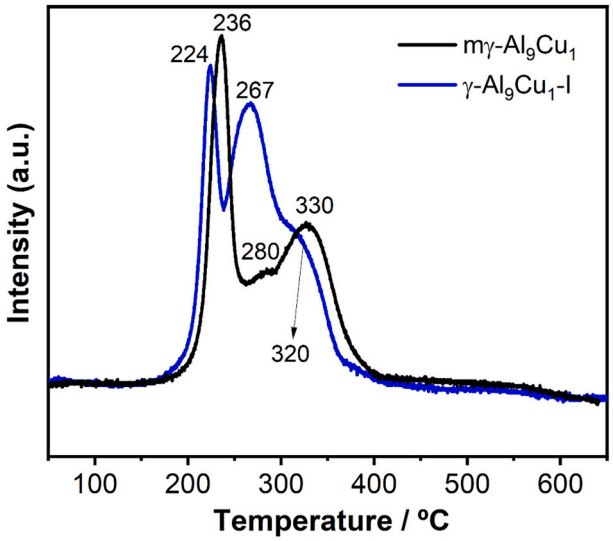

Fig. 5. H_2-TPR profiles for mγ-Al_9Cu_1 and conventional γ-Al_9Cu_1-I catalysts.

process and it appears as a weak shoulder-like feature at around 8985.5 eV (B) in the present study [49]. The absorption band at 9000–9020 eV (D) is due to multiple scattering process, whereas the oscillation at 9030–9080 eV (E) is attributed to single scattering from the nearest-neighbor O atom of Cu [49]. The spectral data in Fig. 7 and edge absorption energy values provided in Table S4 in the supporting information demonstrate that the edge absorption energy of the fresh mγ-$Al_{10-x}Cu_x$-SG catalysts (in the range of 8990.7–8991.9 eV) and conventional γ-Al_9Cu_1-I catalyst (8990.4 eV) is more close to CuO (8990.2 eV), suggesting that copper is in +2 oxidation state in fresh catalysts [49–51]. Moreover, the slope of the edge absorption calculated for γ-Al_9Cu_1-I catalyst is very close to CuO standard and it is relatively less when compared to mγ-$Al_{10-x}Cu_x$-SG catalysts (see Table S4 in the supporting information). In the particular case of mγ-$Al_{10-x}Cu_x$-SG catalysts, the slope of the edge absorption increases as the Cu concentration decreases. With respect to γ-Al_9Cu_1-I catalyst, the slightly increased edge absorption energy value of mγ-$Al_{10-x}Cu_x$-SG catalysts suggests that the copper-alumina interaction in mγ-$Al_{10-x}Cu_x$-SG catalysts is stronger than in γ-Al_9Cu_1-I catalyst and it is in corroboration with the TPR result. Additionally, the amplitude of the oscillation in the region at 9030–9080 eV (E) is reduced much in mγ-$Al_{10-x}Cu_x$-SG catalysts compared to γ-Al_9Cu_1-I catalyst and CuO standard due to higher degree of local structural disorder in the former case.

The Cu K-edge EXAFS spectra of mγ-$Al_{10-x}Cu_x$-SG and γ-Al_9Cu_1-I catalysts, and standard sample of CuO in k space and the corresponding Fourier transformed (FT) spectra in R space are provided in Fig. 8A&B, respectively. The peaks at 1–2 Å in the FT spectra in Fig. 8B corresponds to the bond between Cu and O in the first coordinate shell [10,49]. The peaks in the range of 2–3.2 Å describe the absorbed Cu to nearest Cu coordinate shell distance [49]. The Cu K-edge EXAFS spectral characteristics of γ-Al_9Cu_1-I catalyst in terms of spectral appearance (Fig. 8A) and the Cu—O and Cu-O-Cu peak features in the corresponding FT spectrum (Fig. 8B) is very much resembled to CuO, suggesting that the local structure of Cu species in γ-Al_9Cu_1-I is similar to that of bulk CuO standard [10,46,49]. This infers that the copper species in the γ-Al_9Cu_1-I catalyst interacts weakly with the alumina support due to its bulk-like characteristics. However, in comparison with γ-Al_9Cu_1-I and CuO standard, the Cu K- EXAFS analysis of mγ-$Al_{10-x}Cu_x$-SG catalysts showed dampened EXAFS oscillations in k-space, especially at higher wave numbers (Fig. 8A) and the amplitude of the second shell peak (Cu – O-Cu feature) is significantly less and/or not discernible in the

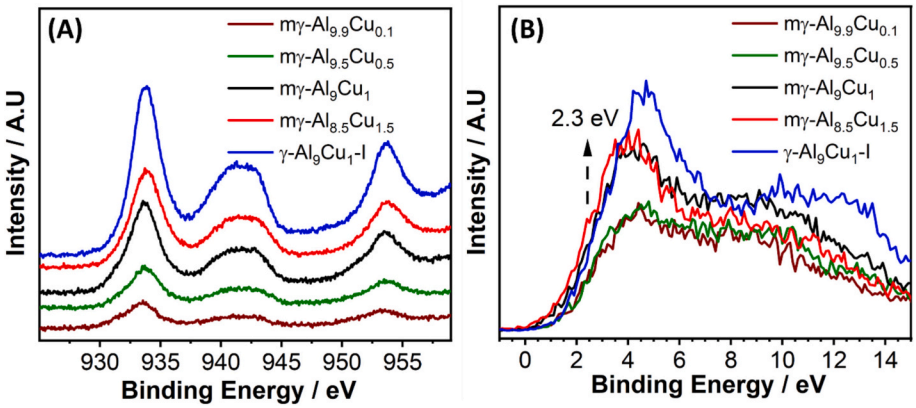

Fig. 6. Cu 2p core level photoelectron spectra (A) and Valence band XPS (B) of fresh mγ-$Al_{10-x}Cu_x$-SG and conventional γ-Al_9Cu_1-I catalysts.

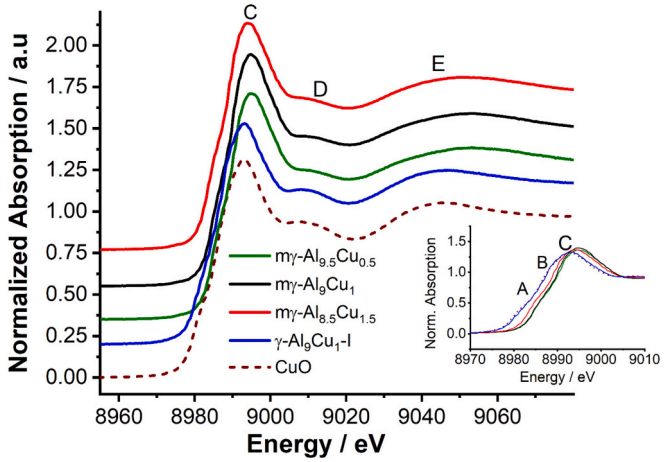

Fig. 7. Cu – K edge XANES spectra of mγ-$Al_{10-x}Cu_x$-SG and conventional γ-Al_9Cu_1-I catalysts (fresh samples), and CuO reference.

corresponding Fourier transformed (FT) spectrum in R-space at 2–3.2 Å (Fig. 8B). This suggests that a long-range structural order was lacking in mγ-$Al_{10-x}Cu_x$-SG catalysts, likely due to the high dispersion of copper species in the alumina lattice resulting a strong copper-alumina interaction imparted by the porous structure [10].

To understand the influence of preparation method on the chemical environment of Cu in the alumina catalysts, EXAFS modeling (fitting) of fresh samples of mγ-Al_9Cu_1 (Fig. 8C) and the conventional γ-Al_9Cu_1-I (Fig. 8D) catalysts were performed. The structural parameters calculated from EXAFS fitting are tabulated in Table S5. The copper species in mesoporous mγ-Al_9Cu_1 showed the best fit when the first shell describing the Cu—O path is only considered for modeling. The Cu—O distance obtained by this fitting model is 1.949 ± 0.01 Å. This distance is very close to the distance calculated for Cu^{2+} species in Cu^{2+} containing catalyst system and CuO standard [10,46,52]. The absence of well discernable EXAFS peak features beyond the first Cu—O path of its fitting spectrum suggests that the copper species are in short-rang order and the remote atoms contribute less significantly to the EXAFS spectra [10]. This infers that copper species in mγ-$Al_{10-x}Cu_x$-SG catalysts are most likely in a highly dispersed state in the mesoporous γ-Al_2O_3 lattice as described in the case of porous Cu/CeO_2/ZSM-5 and Cu/ZSM-5 catalyst systems [10,53]. In contrast to this, the EXAFS modeling of γ-Al_9Cu_1-I indicates that bulk CuO-like species are apparent with Cu—O and Cu—Cu distances of 1.955 ± 0.07 Å and 2.884 ± 0.07 Å, respectively. The fitting parameters calculated for γ-Al_9Cu_1-I are in good match with the values calculated for copper containing catalyst system that show longer-range CuO structure [10,46].

3.4. Catalytic activity

To check the efficacy of mγ-$Al_{10-x}Cu_x$-SG catalysts in the RWGS reaction, we performed activity measurements in the temperature range of 300–600 °C and time-on-stream studies for stability tests at 500 °C at a space velocity (WHSV) of 12,000 mLg^{-1} h^{-1} while maintaining a H_2/CO_2 mole ratio of 4. Control experiments performed on pure mesoporous γ-Al_2O_3 (mγ-Al_2O_3) showed less than 2 % CO_2 conversion in the temperature range of 300-600 °C (Fig. 9), suggesting that an active metal or metal oxide integrated in alumina is essential for improving the CO_2 activation and its further conversion to CO in RWGS reaction. This also ensures the possibility of thermal induced CO_2 conversion to CO is much less over the present catalyst system.

CO_2 conversion obtained for RWGS reaction on mγ-$Al_{10-x}Cu_x$-SG and conventionally prepared γ-Al_9Cu_1-I catalysts at various temperatures is displayed in Fig. 9 (see Table S6 in the supporting information for activity data). Irrespective of the copper concentration, all mγ-$Al_{10-x}Cu_x$-SG catalysts show distinctly higher CO_2 conversion compared to conventional copper catalysts. CO_2 conversion increases as the copper concentration increases while maintaining 100 % CO selectivity in all the cases. For example, mγ-$Al_{10-x}Cu_x$-SG catalysts showed a CO_2 conversion of 27 %, 35 %, 45 %, and 47 % at 500 °C for x values of 0.1, 0.5, 1, and 1.5 respectively. The non-mesoporous conventional γ-Al_9Cu_1-I catalyst was less performing than mγ-$Al_{10-x}Cu_x$-SG under similar experimental conditions and it showed only 16 % CO_2 conversion at 500 °C. It is worth to note that the mγ-$Al_{10-x}Cu_x$-SG catalyst even at lowest copper content (mγ-$Al_{9.9}Cu_{0.1}$, 1.24 wt% Cu or 1 mol% Cu with respect to the total metal content) also showed higher CO_2 conversion than the conventional γ-Al_9Cu_1-I catalyst containing 12.17 wt% of Cu (or 10 mol% Cu). Furthermore, the mesoporous Al_9Cu_1 with almost same Cu loading as that of γ-Al_9Cu_1-I resulted 2.8 times higher CO_2 conversion than γ-Al_9Cu_1-I. These results exemplifies that the present synthesis method is versatile in producing sufficient number of active sites at relatively low copper loading for CO_2 activation and its subsequent reduction by H_2 to CO, and the intrinsic activity of copper species integrated in mγ-$Al_{10-x}Cu_x$-SG catalysts is much higher than the conventionally prepared copper catalyst.

The RWGS reaction performed at various temperatures on mγ-$Al_{10-x}Cu_x$-SG catalysts and γ-Al_9Cu_1-I catalysts revealed that CO_2 conversion and CO production rate increases with reaction temperature for all the catalysts due to the endothermic nature of the reaction. Both mγ-$Al_{10-x}Cu_x$-SG and γ-Al_9Cu_1-I catalysts show 100 % CO selectivity at 300-600 °C, and we could not identify any other side product under the experimental conditions we performed. The mγ-$Al_{10-x}Cu_x$-SG catalysts exhibit distinctly higher CO_2 conversion and CO yield especially at relatively lower temperature than the conventional copper catalyst. CO_2 conversion to CO formation occurs at 300 °C on mγ-$Al_{10-x}Cu_x$-SG catalysts at x ≥ 0.5, whereas for mγ-$Al_{9.9}Cu_{0.1}$, CO production starts at a

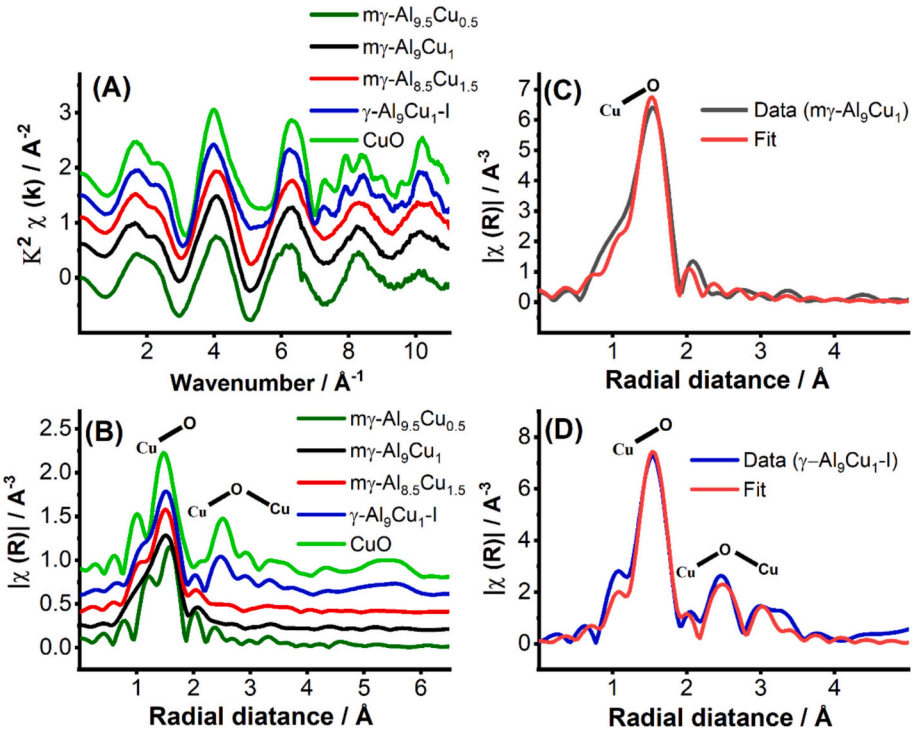

Fig. 8. (A) Cu − K edge EXAFS spectra, and (B) the corresponding Fourier transform (FT) spectra of mγ-$Al_{10-x}Cu_x$-SG and conventional γ-Al_9Cu_1-I catalysts, and CuO reference. EXAFS modeling data of (C) mγ-Al_9Cu_1, and (D) conventionally prepared γ-Al_9Cu_1-I catalysts.

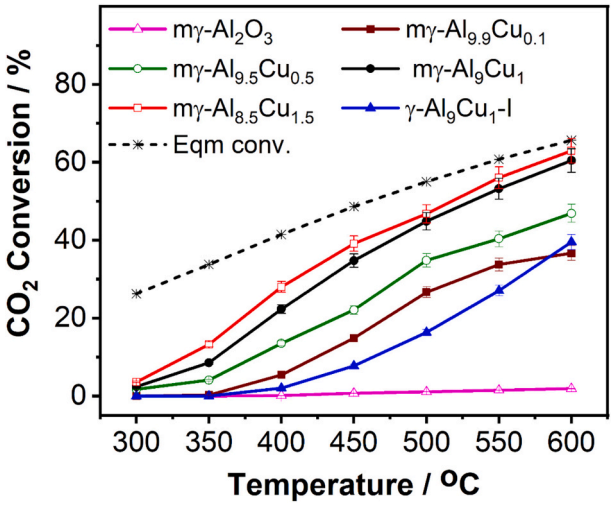

Fig. 9. CO_2 conversion on mγ-$Al_{10-x}Cu_x$-SG and conventional γ-Al_9Cu_1-I catalysts at various temperatures (reaction conditions: 100 mg catalyst, H_2/CO_2 mole ratio = 4, WHSV = 12,000 mL·g^{-1}·h^{-1}).

slightly higher temperature of 350 °C. For example, mγ-Al_9Cu_1 showed a CO_2 conversion of 2.4 % at the reaction temperature of 300 °C, which is increased to 22.3 % at 400 °C, 45 % at 500 °C and 60.4 % at 600 °C. The conventional γ-Al_9Cu_1-I catalyst, on the other hand, didn't show any activity up to 350 °C. The γ-Al_9Cu_1-I catalyst could achieve a CO_2 conversion of only 2 %, 16.3 % and 39.5 % at 400 °C, 500 °C, and 600 °C, respectively. We also performed RWGS reaction on mγ-$Al_{10-x}Cu_x$-SG catalysts without any pre-reduction treatment and found that the catalysts in unreduced conditions are also active with a maximum of 6.6 % decline in the activity with respect to the parent sample for all the compositions and at all temperatures while maintaining 100 % CO selectivity (see Fig. S4 in the supporting information). This is an added advantage of the present catalyst system that the pre-activation step often needed for the reaction can be avoided, which can minimize the overall process cost, and it is relevant in real industrial applications.

The catalytic performance of mγ-$Al_{10-x}Cu_x$-SG and γ-Al_9Cu_1-I catalysts were carried out by performing time-on-stream (TOS) for a period of 50 h at 500 °C and WHSV of 12,000 mLg^{-1} h^{-1} to check the stability of the catalyst, and the results are shown in Fig. 10 (see Table S7 in the supporting information for activity data). The mγ-$Al_{9.9}Cu_{0.1}$ catalyst displayed excellent stability with a CO_2 conversion of 26–28 % and no detectable deactivation throughout the 50 h of activity study. Interestingly, mγ-$Al_{10-x}Cu_x$-SG catalysts with higher Cu loading also displayed high activity with comparatively less decline in the CO_2 conversion as time progresses. For example, mγ-Al_9Cu_1 (12.17 wt% Cu) showed a CO_2

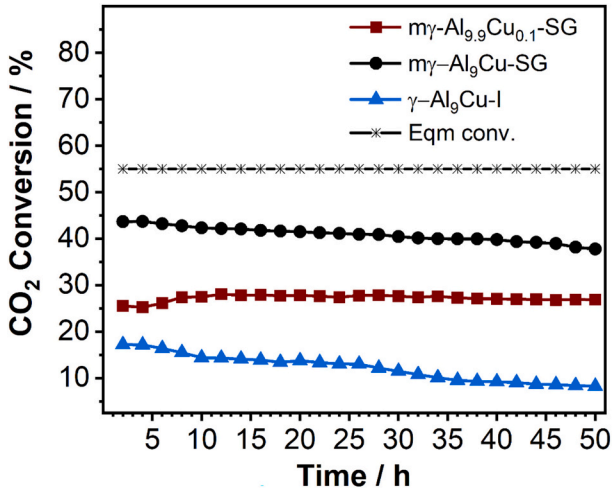

Fig. 10. Stability test by TOS study on mγ-$Al_{9.9}Cu_{0.1}$, mγ-Al_9Cu_1 and conventional γ-Al_9Cu_1-I catalysts at 500 °C (reaction conditions: 100 mg catalyst, H_2/CO_2 mole ratio = 4, WHSV = 12,000 mL·g^{-1}·h^{-1}).

conversion of 43.7 % in the second hour of the reaction and it is decreased to 37.8 % after 50 h of time on stream (Fig. 10), whereas mγ-$Al_{8.5}Cu_{1.5}$ catalyst with more Cu loading resulted a CO_2 conversion of 44.5–40.3 % with only a 4 % decrease of CO_2 conversion in the 30 h TOS study (not shown). All these catalysts show a CO selectivity of 100 % and no side products such as CH_4 were detected during the entire period of study. In comparison, the conventional reference γ-Al_9Cu_1-I catalyst showed only 17.2 % CO_2 conversion in the second hour, which is decreased to 8.2 % after 50 h period though the CO selectivity is 100 % throughout the TOS study. Compared to the mγ-Al_9Cu_1 catalyst that lost only 13.5 % of its initial activity after 50 h, the conventional γ-Al_9Cu_1-I catalyst with same Cu content as that of mγ-Al_9Cu_1 catalyst lost 52.3 % of its initial activity after 50 h. The hydroxyl groups on the alumina surface act as anchoring sites for Cu species and thereby play a decisive role in determining the nature of the Cu-Al_2O_3 interaction and the distribution of copper species, which influences the stability and catalytic efficiency of mγ-$Al_{10-x}Cu_x$-SG catalysts. mγ-$Al_{9.9}Cu_{0.1}$ containing maximum amount of surface hydroxyl group and lowest Cu loading promote high dispersion of Cu species on the alumina surface with high binding strength of copper species to the alumina support, resulting high catalyst stability though it shows relatively less CO_2 conversion rate due to low Cu content in it. The present study also demonstrates that the conventional γ-Al_9Cu_1-I catalyst with a higher copper concentration and lowest quantity of surface hydroxyl group on the alumina surface is less effective in stabilizing Cu particles and as a result sintering of Cu particles occurs and the catalyst deactivates fast during the RWGS reaction at higher reaction temperature. Compared to conventional γ-Al_9Cu_1-I catalyst, mγ-Al_9Cu_1 catalyst with relatively more surface hydroxyl group could stabilize more Cu particles, which enhances the stability of the catalyst.

Despite the low affinity of Cu metal for H_2 and high vulnerability of Cu catalysts to sintering at high temperature, continuous efforts have been made in the literature in developing Cu-based catalysts for RWGS reaction and a comprehensive analysis of these catalysts and advances in their development is addressed in a recent review [20]. A comparison of the activity of mγ-$Al_{10-x}Cu_x$-SG catalysts in this study with various Cu-based catalysts reported in the literature is provided in Table S8 in the supporting information. The RWGS reaction activity of mγ-$Al_{10-x}Cu_x$-SG catalysts in this study are highly promising than most of the Cu-based catalysts such as Cu catalysts produced by different preparation methods, Cu catalysts supported on irreducible and reducible oxide supports and various other substrates [2,9–20], Cu-incorporated zeolites and mesoporous silica [10,19], Cu—Al spinel catalysts [17], Cu-based layered double hydroxides (LDHs) [18], and Cu catalysts in combination with other secondary metal component as promoter or additive [2,11,20] (see Table S8 in the supporting information). Particularly, as shown in Table S8, compared with the previously reported Cu/Al_2O_3 catalysts with Cu content comparable in the range of the present catalyst system, mγ-$Al_{10-x}Cu_x$-SG catalysts showed excellent catalytic performance in terms of activity and stability. Moreover, under similar experimental conditions, mγ-$Al_{10-x}Cu_x$-SG catalysts displayed remarkably high CO_2 conversion rate and stability than the conventional γ-Al_9Cu_1-I catalyst in this study. With respect to the Cu/Al_2O_3 catalysts reported in the literature, the high catalytic performance of mγ-$Al_{10-x}Cu_x$-SG catalysts in this study is likely due to fine dispersion of Cu nanocrystallites in the mesoporous γ-Al_2O_3 frame work and its stabilization by surface hydroxyl group furnished by mesoporous alumina, resulting in an increased number of surface-active sites for adsorption and reaction.

3.5. Characterization of spent catalysts and structure-activity relation

The structure-activity study of mγ-$Al_{10-x}Cu_x$-SG and γ-Al_9Cu_1-I catalysts revealed that the Cu loading and surface heterogeneity such as the distribution of Cu and the nature of oxygen species surface morphology and porosity, Cu-Al_2O_3 interaction and the nature of active sites at the Cu-Al_2O_3 interface, and the electronic characteristics of the Cu species in due course of the reaction play crucial roles in the RWGS reaction activity, CO selectivity and stability. The relatively high CO production rate and stability of mγ-$Al_{10-x}Cu_x$-SG catalysts in comparison with the conventional γ-Al_9Cu_1-I catalyst exemplifies that the activity and stability of copper sites is enhanced in mγ-$Al_{10-x}Cu_x$-SG catalysts. This is due to the fine distribution of Cu species in the mesoporous alumina lattice, modified metal-alumina interface, and the strong metal-support (copper-alumina) interaction as evidenced from XRD, SEM/TEM, XPS and Cu K-edge XAS studies. Additionally, the porous characteristics of the material reduces the diffusion limitation of the reactants and products, avoid the pressure drop problem during catalysis and also offers a spatial confinement effect to the active CuO_x species, which could enhance the overall catalytic performance by retarding the agglomeration of Cu particles during the course of the reaction.

The nature of interaction between the reactant molecules (CO_2 and H_2) and the catalyst surface, the charge transfer property of the catalyst as well as the relative amount of the active components at the copper-alumina interface are decisive in the activation and dissociation of CO_2 and H_2, and their subsequent reduction pathway to CO. To know the electron transfer dynamics and the relative number of active sites at the Cu-Al_2O_3 interface, electrochemical properties of mesoporous Al_9Cu_1 and conventional γ-Al_9Cu_1-I catalysts were studied by electrochemical impedance spectroscopy (EIS) and cyclic voltammetry (CV) (see supporting information for details). The Nyquist plot obtained from EIS and CV curves of mγ-Al_9Cu_1 and conventional γ-Al_9Cu_1-I catalysts are shown in Fig. S5 and Fig. S6, respectively. The apparently smaller R_{ct} value of mesoporous Al_9Cu_1 compared to conventional γ-Al_9Cu_1-I catalyst indicates the faster charge transfer efficiency and higher conductivity of the mγ-Al_9Cu_1 catalyst. The voltametric charge (Q) obtained from the CV curve is used to determine the number of surface-active sites(n), which can be correlated to the activity of the catalyst in RWGS reaction. The Q and the corresponding 'n' values of the mγ-Al_9Cu_1 (0.1055C and 5.47×10^{-7} mol) was comparatively higher than the γ-Al_9Cu_1-I catalyst (0.0363C and 1.88×10^{-7} mol), implying that mγ-Al_9Cu_1 with large number of surface-active sites are more efficient than conventional γ-Al_9Cu_1-I catalyst in RWGS reaction.

Further information on the surface heterogeneity in terms of Cu distribution and relative amount of oxygen species, and a corroboration of it with RWGS activity was obtained from XPS analysis. The Cu/Al and O_H/O_L ($O_{Hydroxyl}/O_{Lattice}$) ratios calculated from XPS analysis is plotted against the catalyst composition in Fig. 11. Catalyst surface either enriched with hydroxyl group or Cu species is not good for the reaction. For example, mγ-$Al_{9.9}Cu_{0.1}$ catalyst with relatively high concentration of hydroxyl group and low Cu content shows poor activity. Similarly,

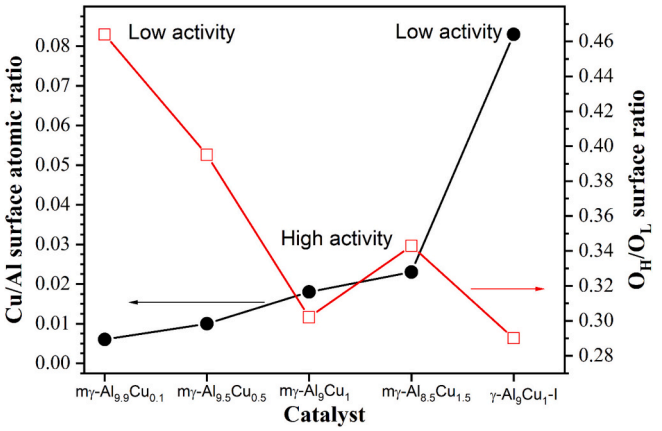

Fig. 11. Correlation of Cu/Al and $O_{Hydroxyl}/O_{Lattice}$ (O_H/O_L) surface atomic ratio and RWGS reaction activity of mγ-$Al_{10-x}Cu_x$-SG and conventional γ-Al_9Cu_1-I catalysts. Cu/Al and O_H/O_L surface atomic ratio obtained from XPS was plotted.

γ-Al_9Cu_1-I catalyst surface with more Cu content show poor activity. From the Fig. 11 and activity results, it is clear that an optimum amount of surface hydroxyl and Cu species on the catalyst surface is good for better activity in RWGS reaction. These results suggest that the number of surface active sites available for CO_2 adsorption and activation, and subsequently its reduction by H_2 to CO decreases if alumina surface is covered with more Cu species [20,26]. The relatively lower CO_2 conversion on γ-Al_9Cu_1-I is likely due to this hypothesis. The mγ-$Al_{10-x}Cu_x$-SG catalysts (mγ-Al_9Cu_1 and mγ-$Al_{8.5}Cu_{1.5}$) with uniform distribution of surface hydroxyl group and Cu species in an optimum concentration exhibited the highest activity.

To understand the critical changes happened to the catalyst materials after the reaction, characterization of the spent catalysts of mγ-Al_9Cu_1 and the γ-Al_9Cu_1-I catalysts obtained after stability study at 500 °C were carried out. XRD pattern of the spent catalyst of conventional γ-Al_9Cu_1-I catalyst show sharp and intense reflections characteristic of metallic copper (Fig. S7 in the supporting information). The comparatively large activity decline observed in the case of conventional γ-Al_9Cu_1-I catalyst as time progresses is likely due to the segregation of Cu nanoparticles into bulk agglomerates under the reaction conditions [10]. Contrarily, the broad peak observed at 2θ =30-40° in the fresh catalyst of mγ-Al_9Cu_1 has become more sharp with very weak reflections of metallic Cu at 2θ =43.248° (JCPDS No. 4-836) in the corresponding spent catalyst. This suggests that the Cu species were not segregated much, and they are in a highly dispersed state and still exists as fine particles in mγ-Al_9Cu_1 [26]. The enhanced charge transfer and the electrochemically more active sties at the copper-alumina interface, and the strong metal (Cu)-support (Al_2O_3) interaction in mγ-Al_9Cu_1 modify the electronic structure of Cu species, enhances the Cu dispersion, and suppress the segregation of Cu nanoparticles into bulk agglomerates during the reaction, which accounts for its enhanced activity and stability in comparison with conventional γ-Al_9Cu_1-I catalyst [2].

Cu 2p XPS analysis of mγ-Al_9Cu_1 and γ-Al_9Cu_1-I catalysts obtained after RWGS reaction provided clear evidence of the Cu^{2+} reduction during the RWGS reaction (Fig. 12A). The deconvolution analysis of the $Cu2p_{3/2}$ peaks of the spent mγ-Al_9Cu (γ-Al_9Cu_1-I) catalysts showed two BE components at 933.5 (933.7) eV and 931.9 (932) eV. The high BE component at 933.5 (933.7) eV is due to Cu^{2+} species, whereas the low BE component at 931.9 (932) eV is due to reduced Cu species (Cu^+ and Cu^0) [17,26,43]. The evidence of an intense satellite feature at around 943 eV supports the presence of Cu^{2+} species in the spent mγ-Al_9Cu and γ-Al_9Cu_1-I catalysts, indicating that part of the reduced copper species must have reoxidized during the reaction process [26]. The literature evidence suggests that the BE component at 932 eV is not discernible to discriminate Cu^+ and Cu^o species [17,26,43]. A higher percentage of reduced Cu species on the γ-Al_9Cu_1-I surface (51 %) compared to mγ-Al_9Cu_1 surface (39 %) indicating that the Cu^{2+} species in γ-Al_9Cu_1-I is reduced more during the reaction. Moreover, the FWHM of the Cu $2p_{3/2}$ peak component of the spent catalyst of γ-Al_9Cu_1-I (3.63 eV) is higher than the corresponding fresh catalyst (2.34 eV), and the spent catalyst of mγ-Al_9Cu (3.23 eV). The above results hint that the peak component around 932 eV is comprised of both Cu^0 and Cu^+ species [43].

To distinguish Cu^+ and Cu^0 species in the spent samples, X-ray-induced Auger electron spectroscopic analysis of spent mγ-Al_9Cu_1 and γ-Al_9Cu_1-I catalysts were performed and the spectral results are shown in Fig. 12B. It can be seen from the Cu LMM Auger spectra that both the spent catalysts exhibit Cu LMM Auger components at KE values of 916.5, 917.6, 918.9, which are assigned to Cu^{+1}, Cu^{+2}, and Cu^0, respectively [25,43,54]. In contrast to spent mγ-Al_9Cu_1 catalyst, the KE component corresponding to Cu^0 at 918.9 eV on spent γ-Al_9Cu_1-I catalyst is relatively sharp with less broadening. This clearly indicates the contribution of Cu^0 is high on the conventional spent γ-Al_9Cu_1-I catalyst, which underlines the results obtained from XRD and Cu 2p XPS analysis. However, a reliable estimation of each Cu component is difficult due to a large overlap of the Auger peaks with a significant background in the spectra [43].

The VB XPS spectra of the spent Al_9Cu_1 and γ-Al_9Cu_1-I catalysts provide further evidence on the surface electronic structure of Cu species on the catalyst surface (Fig. 12 C) [46]. Besides the main Cu 3d band at 4–4.5 eV and broad low intense O 2p features at 4.5–7.5 eV, a new VB

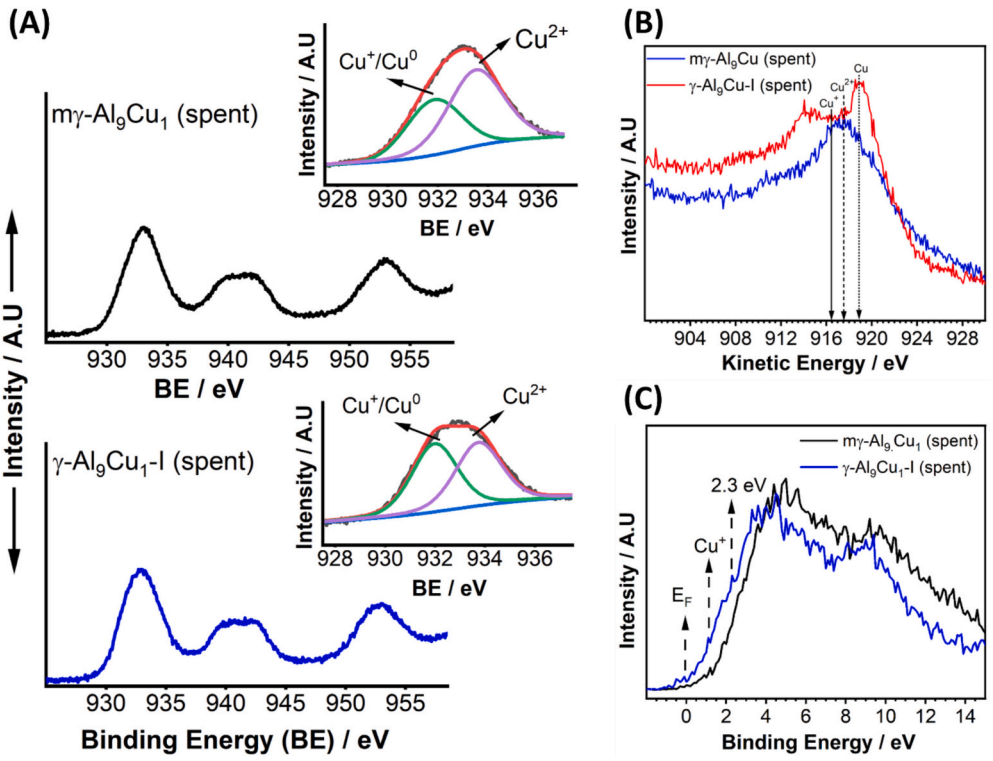

Fig. 12. Cu 2p core level XPS spectra (A), Cu LMM Auger electron spectra (B), and Valence band XPS spectra (C) of spent mγ-Al_9Cu_1 and conventional γ-Al_9Cu_1-I catalysts.

feature appears at 1.3 eV in the spent catalysts of Al_9Cu and γ-Al_9Cu_1-I, which is characteristic of Cu_2O species [25]. The relatively weak satellite peak observed at 9–12.5 eV for the spent catalysts is attributed to Cu^{2+} species [25,43]. Interestingly the VB spectra of the spent catalyst γ-Al_9Cu_1-I show a shoulder around 2.3 eV, which is similar to that of bulk CuO [46]. However, this shoulder peak is very weak or absent in the spent mγ-Al_9Cu_1 catalyst, suggesting that the aggregation and particle growth of Cu species are very much high in conventionally prepared γ-Al_9Cu_1-I catalyst. The VB spectra of the spent mγ-Al_9Cu_1 and γ-Al_9Cu_1-I catalysts also show a low intense BE feature at Fermi level (0 eV), the intensity of which is more pronounced in γ-Al_9Cu_1-I and it is due to the Fermi level (E_F) of metallic Cu species [55,56]. VB XPS spectra given in Fig. 12C agrees with XRD and Cu 2p core level XPS results.

Further evidence of severe aggregation of Cu species in γ-Al_9Cu_1-I compared to mγ-Al_9Cu_1 during the reaction was obtained from XPS by comparing the Cu/Al atomic ratio between the fresh and spent samples. The Cu/Al surface atomic ratio calculated for spent γ-Al_9Cu_1-I catalyst showed a value of 0.020, which is about 76 % decrease with respect to the value of 0.083 in the corresponding fresh catalyst. Contrarily, the Cu/Al surface atomic ratio on mγ-Al_9Cu_1 was increased to 0.029 in the spent catalyst from an initial value of 0.018 in the fresh catalyst, suggesting that mesoporous structure in mγ-$Al_{10-x}Cu_x$-SG catalysts allow redispersion of Cu species without any particle growth during the reaction. These results exemplify a remarkable change in the electronic structure of Cu species on the spent catalysts surface with respect to the fresh catalysts. We have performed in situ XPS analysis under NAP-XPS conditions (typically ~0.1 mbar of the reactive gas environment) to obtain more reliable information about O_H/O_L surface atomic ratio, oxidation states and relative proportion of various surface Cu species in real reaction conditions in the presence of H_2, CO_2 and H_2/CO_2 mixtures. However, the intrinsic charging of this material resulted a charging-induced shift of approximately 36 eV, limiting its suitability for in situ NAP-XPS analysis at elevated pressures (see supporting information for details).

The Cu K-edge XANES and EXAFS analysis of the spent catalyst of mγ-Al_9Cu_1 was carried out and compared with the corresponding fresh catalyst and other standard copper oxides including CuO and Cu_2O to understand the oxidation state of Cu and the structural changes happened to the catalyst after the RWGS reaction (Fig. 13A). The edge energy value of the spent mγ-Al_9Cu_1 catalyst (8989.06 eV) in the XANES spectra in the inset of Fig. 13A was about 1.2 eV less than with respect to the corresponding fresh catalyst and it is in between CuO and Cu_2O. This further confirms the reduction of CuO species occurs during the RWGS reaction. Nonetheless, we could not observe any large difference in the XANES and EXAFS spectra between fresh and spent catalysts (Fig. 13B&C). Further, a comparison of the curve-fitting analysis of the spent and fresh Al_9Cu_1 catalyst confirmed that the local structure of the Cu species in the spent catalyst is essentially the same as that of the fresh sample though the Cu-O-Cu peak feature in the spent catalyst is slightly grown (Fig. 13D). The above results underscore that there is not much variation in the local environment of copper species in mγ-Al_9Cu_1, and the structural integrity of the catalyst was maintained during the reaction.

3.6. DFT study of the RWGS reaction on Cu (111) and Cu/γ-Al_2O_3(110) surfaces

Density functional theory (DFT) calculations were performed to explore the RWGS reaction mechanism on the catalyst surfaces of Cu (111) and Cu/γ-Al_2O_3(110). The bulk structures of Cu (mp-30) and γ-Al_2O_3 (mp-1143) were taken from the materials project database. Then the stable surface terminations were cleaved for Cu (111) and γ-Al_2O_3(110). We used these two slab models to study the RWGS reaction mechanism ($CO_2 + H_2 \rightarrow CO + H_2O$). The reaction free energy profile is shown in Fig. 14. The reaction is initiated by adsorption of reactants CO_2 and H_2 on the surfaces. The CO_2 molecule is only physically adsorbed over Cu (111) (E_{ads} = 0.68 eV), while it is chemically adsorbed over Cu/γ-Al_2O_3 (110) (E_{ads} = −1.51 eV). On the other hand, H_2 is weakly physisorbed (E_{ads} = 0.48 eV) in both cases. Subsequently, the adsorbed H_2 molecule is activated to produce surface adsorbed H

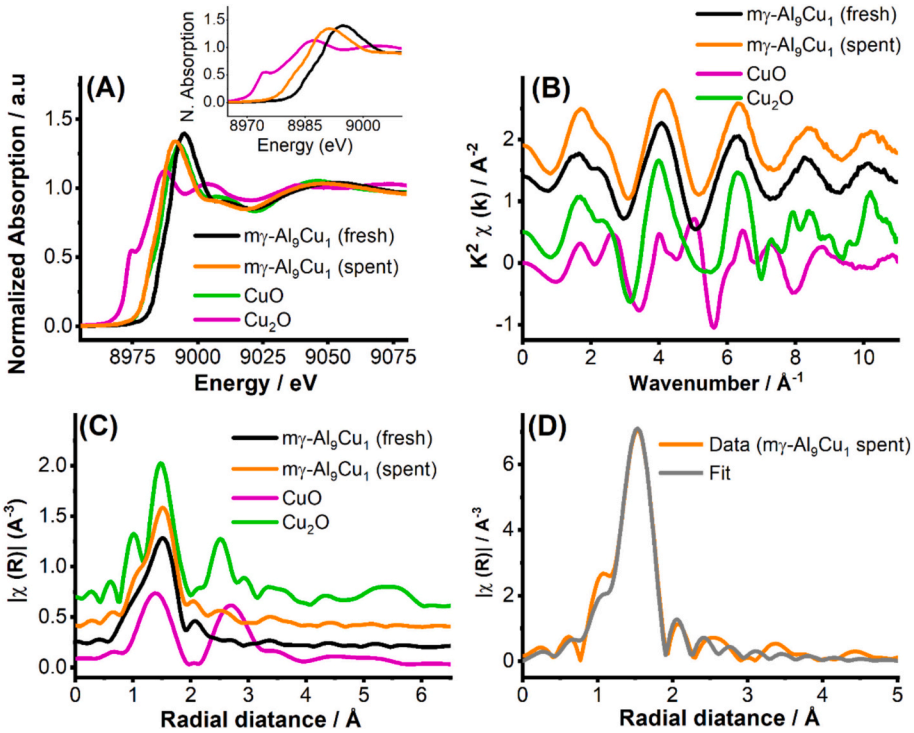

Fig. 13. (A) Cu − K edge XANES spectra of fresh and spent mγ-Al_9Cu_1 catalysts and reference samples (CuO and Cu_2O). (B) Cu − K edge EXAFS spectra, and (C) the corresponding Fourier transform (FT) spectra of fresh and spent mγ-Al_9Cu_1 catalysts and reference samples (CuO and Cu_2O). (D) EXAFS modeling data of spent mγ-Al_9Cu_1 catalyst.

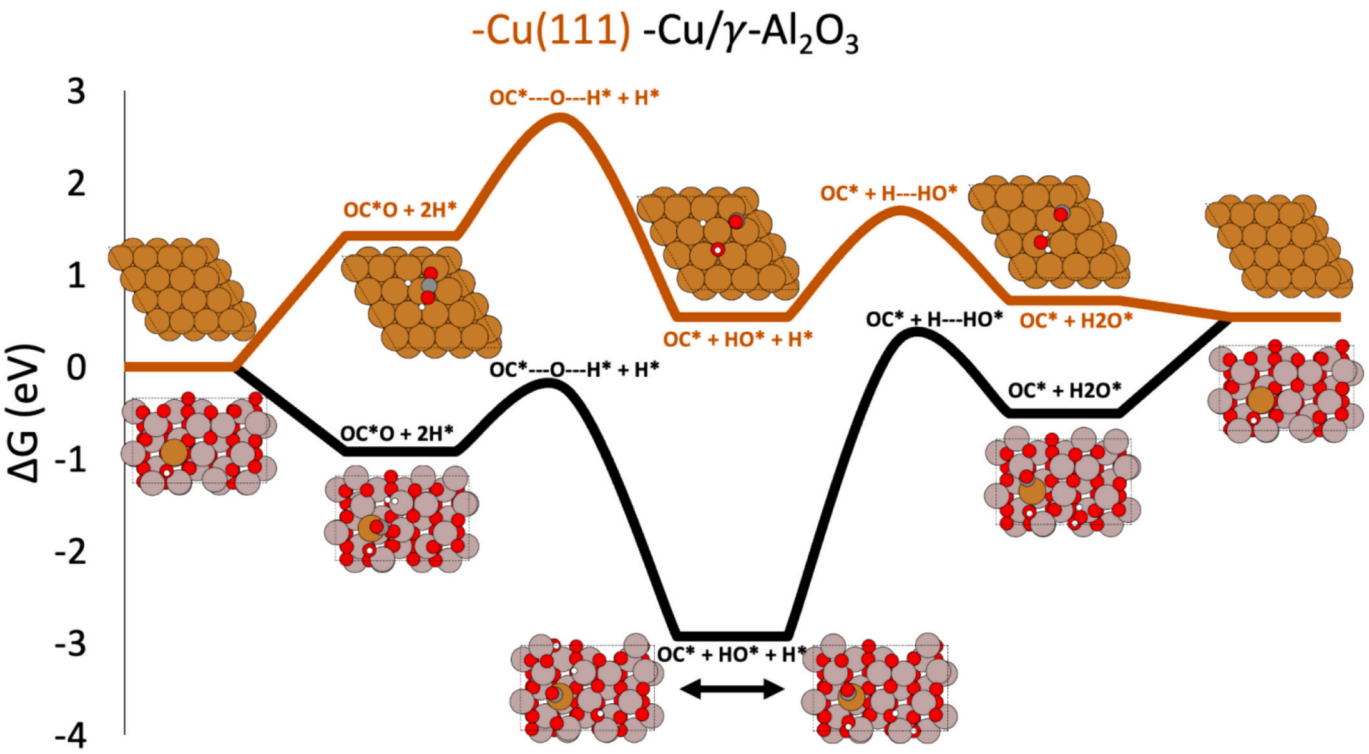

Fig. 14. The calculated reaction free energy profile of the COOH pathway of the reaction mechanism for the RWGS reaction on the Cu (111) and Cu/γ-Al_2O_3(110) surfaces. The reaction free energy profile in reddish brown and black colors indicate the reaction pathway on Cu (111) surface, and Cu/γ-Al_2O_3(110) surface, respectively.

species (H*), and the C—O bond of CO_2* is activated by H* to produce CO* and OH*. In the case of Cu (111), this process is thermodynamically and kinetically much more energy demanding (E_a = 1.28 eV; ΔE = −0.88 eV) compared to that over Cu/γ-Al_2O_3 (110) surface (E_a = 0.67 eV; ΔE = −2.01 eV). The next step in the process is water formation (OH* + H* → H_2O*). In the case of Cu (111), this step has an activation barrier of 1.15 eV and reaction energy of 0.17 eV; however, the same reaction step over Cu/γ-Al_2O_3 (110) is rather difficult (E_a = 3.22 eV; ΔE = 2.42 eV). The last step of CO* and H_2O* desorption is facile for both models. Overall, DFT calculation indicates that RWGS reaction is

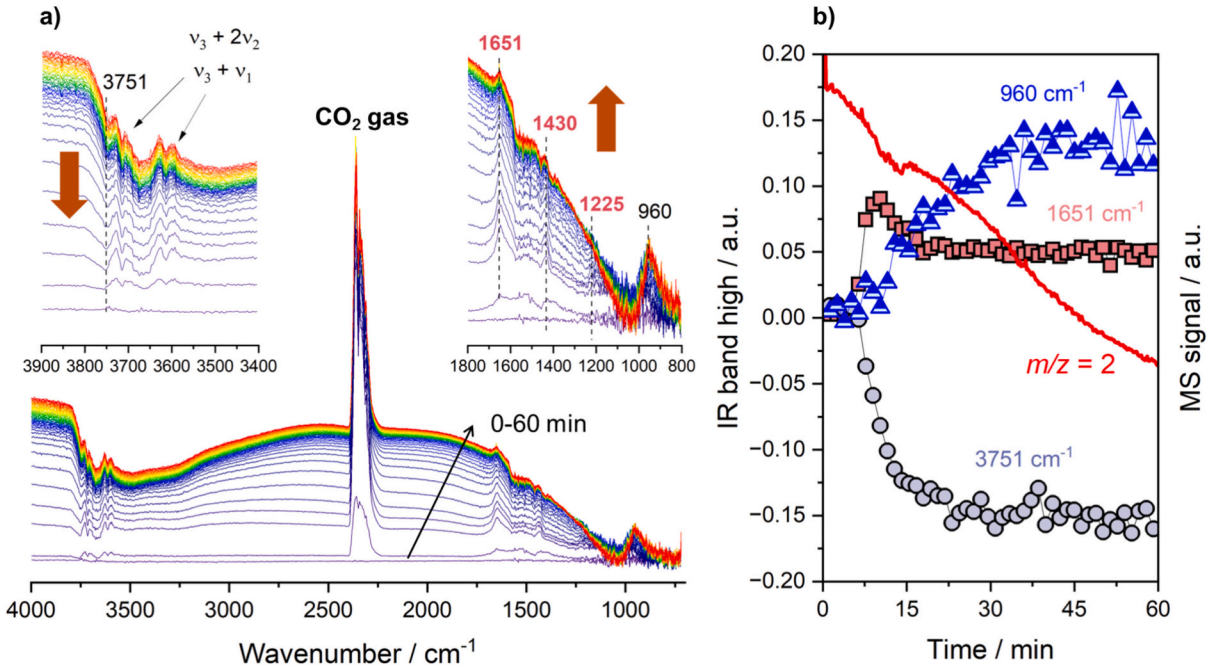

Fig. 15. (a) Temporal evolution of *operando* DRIFTS spectra recorded during the RWGS reaction over mγ-Al_9Cu_1 catalyst. Reaction conditions: P = 1 bar, T = 300 °C, H_2:CO_2:Ar = 4:1:1, and total flow rate of 60 mL/min (b) Evolution of the main bands related to surface species involved in the reaction and evolution of the m/z = 2 signal (H_2) followed on-line by MS.

thermodynamically favorable over Cu/γ-Al_2O_3 (110) compared to Cu (111) catalytic surface.

3.7. Operando DRIFTS-MS analysis of RWGS over mγ-Al_9Cu_1 catalyst

The mγ-Al_9Cu_1 catalyst was selected to gain further details about the species involved in the RWGS mechanism using *operando* DRIFTS-MS measurements. We hypothesize that the reaction occurs through the formation of hydroxycarbonyl intermediates which are rapidly decomposed into CO and H_2O. In this pathway, the redox pair $Cu^0/Cu^{\delta+}$ plays a key role. Nevertheless, these intermediates are very unstable and can be hardly detected by DRIFTS. To confirm this hypothesis, the experiment was carried out at 300 °C to minimize overall conversion, thereby enabling the investigation of CO_2 activation under conditions of limited reactivity. Additionally, the catalyst was pretreated in the absence of hydrogen to maintain the Cu^{2+} oxidation state or to allow only partial reduction.

Fig. 15 displays the time-resolved spectra recorded as a function of time-on-stream for mγ-Al_9Cu_1 catalyst. As can be observed, three spectral features were developed at 1225, 1430 and 1651 cm^{-1} suggesting the formation of surface bicarbonates [57]. Although the 3800–3300 cm^{-1} is partially masked by the characteristic combination modes ($\nu_3 + 2\nu_2$) and ($\nu_3 + \nu_1$) of gaseous CO_2 [58], it is clearly observed that a band at 3751 cm^{-1} vanished with the reaction time. This feature is assigned to aluminium bonded terminal hydroxyl species [59]. It is well known that bicarbonate formation on an oxide surface occurs from the reaction between CO_2 and the surface hydroxyl groups. Such an interaction has been typically observed on alumina, where it was found that reaction takes place with the highest wavenumber of hydroxyls [60]. Likewise, Song et al. [61] reported that terminal hydroxyl groups are the involved species in the CO_2 activation. Busca and Lorenzelli proposed that bicarbonate can adsorb as either monodentate or bidentate structures on the surface of metal oxides [57] although in alumina more typically observed are the monodentate species.

Moreover, a broad band centered at 960 cm^{-1} is also observed. Some studies have shown that monodentate and bidentate bicarbonate species can exhibit bands in the ~960–980 cm^{-1} region, which are assigned to bending or torsional modes [62]. The intensity of these bands is typically weak to moderate compared to the strong band observed at 1225 cm^{-1}. In our case, the emergence of the band at 960 cm^{-1} suggests that the bicarbonate species could become highly distorted, or that it is activated, forming a non-conventional surface intermediate. As shown in Fig. 15b, the IR profiles clearly reveal that hydroxyl groups disappeared while bicarbonate species were simultaneously formed. Additionally, it is noteworthy that the band at 960 cm^{-1} emerged precisely after hydrogen consumption, in concordance with the negative peak observed at $m/z = 2$ signal of mass spectrometer. According to the TPR results (Fig. 5), it is reasonable to assume that Cu^{2+} is reduced to Cu^+ at a temperature of 300 °C and the band at 960 cm^{-1} could be related to O-$Cu^{\delta+}$ stretching vibrations [63]. Therefore, it can be stated that ions Cu^{2+} were partially reduced during the reaction to form new Cu entities, which acted as adsorbed H_2 sources for the transformation of the adsorbed CO_2 on the Cu—Al surface. In agreement with Song et al. [61], the exposure of Cu active sites can be facilitated by H pre-adsorption or co-adsorption, which simultaneously promotes the formation of carbon-containing intermediates. We speculate that to the formation of local reduced copper hydroxycarbonate species analogous to azurite and/or malachite phases can act as active phase for low temperature reverse water gas shift reaction as was recently reported by our group [64]. In other study, Jiang et al. [65] demonstrated copper carbonate hydroxide resembling the mineral malachite acts as a precursor of interfacial CO during CO_2 electroreduction. Based on all these observations, we propose that CO_2 is activated on the hydroxyl groups of alumina, forming a monodentate bicarbonate which, in the presence of partially reduced copper, undergoes a restructuring to form a species that could be the precursor of hydroxycarbonyl-type intermediates as sketched in Scheme 2. In the classical associative mechanism, it has been proposed that bicarbonate-type species are reduced to formates, which then decompose into CO and water. Herein, the apparent absence of formates — that typically require high temperatures for decomposition — suggests that optimal low-temperature RWGS catalysts follow alternative pathways involving thermally less stable intermediates, such as the one proposed here.

During CO_2 adsorption and activation, alumina acts not only as a support but also as an electron acceptor. This additional role enhances the electrostatic interaction between the copper active centers and the negatively charged oxygen atoms of CO_2, thereby facilitating the activation of the C—O bonds. This synergistic effect has been also demonstrated by means of DFT calculations concluding that the interaction between the Al_2O_3 support and small clusters of copper is crucial for effective CO_2 activation [66].

3.8. The RWGS reaction mechanism

Based on the reaction pattern, DFT calculation on Cu/γ-Al_2O_3, and *Operando* DRIFTS-MS analysis of RWGS reaction over mγ-Al_9Cu_1 catalyst in this study and the literature evidences of various metal doped oxide catalyst system [67–69], the mechanism for CO production is proposed to be $CO_2 + H_2 \rightarrow OCOH \rightarrow CO + H_2O$ via the formation of hydroxycarbonyl intermediate and accomplished through different steps as illustrated in Scheme 3. The RWGS reaction is initiated by adsorption of CO_2 and H_2 molecules on Cu/γ-Al_2O_3 surface, subsequently their activation to form surface CO_2* and H* species (Eqs. (6)–(7)). As previously reported for the case of oxide supported metal catalysts [67–69], we believe that the copper-alumina interface plays crucial roles in the activation of CO_2 and H_2 though Cu nanoparticles directly don't have any role in the activation of CO_2. In the second step, the C—O bond of surface adsorbed CO_2* in its first stage of reduction process react with adsorbed H species (H*) to form hydroxycarbonyl (O=C*-OH) intermediates at the copper-alumina interface (Eq. (8)). The hydroxycarbonyl (O=C*-OH) species are then decomposed to form CO* and OH* in the third step (Eq. (9)). Subsequently, in the fourth step, water formation ($OH^* + H^* \rightarrow H_2O^*$) occurs by the reaction between OH* and the remaining surface H* and complete the overall CO_2 reduction process (Eq. (10)). Desorption of surface CO* and H_2O* occurs in the final step of the reaction cycle (Eqs. (11)–(12)). The strong metal-oxide interaction in mγ-$Al_{10-x}Cu_x$-SG catalysts stabilizes the Cu nanoparticles in the γ-Al_2O_3 lattice, which enhances the adsorption and dissociation of hydrogen and CO_2 activation. Consequently, formation of more hydroxycarbonyl species occurs on mγ-AlCu materials, which enhances the RWGS activity.

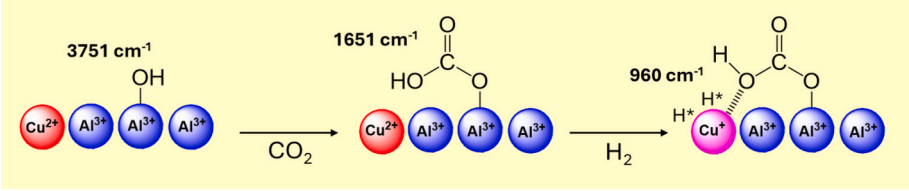

Scheme 2. Proposal of hydroxycarbonyl precursor intermediate on mγ-Al_9Cu_1 catalyst.

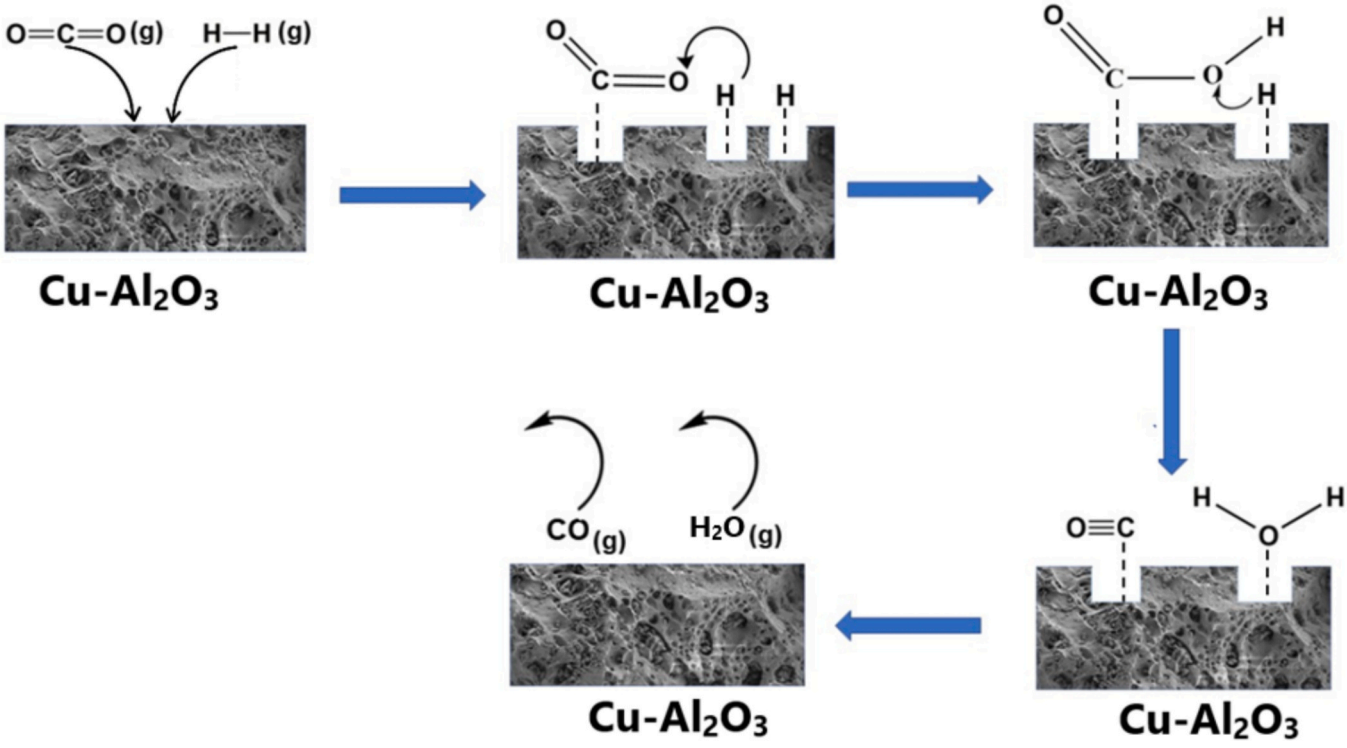

Scheme 3. Proposed associative mechanism of RWGS reaction on mγ-$Al_{10-x}Cu_x$-SG catalysts.

$$O = C = O(g) \rightarrow O = C^* = O_{ads} \quad (6)$$

$$H_2(g) \rightarrow 2H^*_{ads} \quad (7)$$

$$O = C^* = O_{ads} + H^*_{ads} \rightarrow O = C^* - O - H^*_{ads} \quad (8)$$

$$O = C^* - O - H^*_{ads} \rightarrow CO^*_{ads} + OH^*_{ads} \quad (9)$$

$$OH^*_{ads} + H^*_{ads} \rightarrow H_2O^*_{ads} \quad (10)$$

$$CO^*_{ads} \rightarrow CO(g) \quad (11)$$

$$H_2O^*_{ads} \rightarrow H_2O(g) \quad (12)$$

4. Conclusions

We report a simple and robust sol-gel synthesis strategy to prepare mesoporous $Al_{10-x}Cu_xO_y$ (mγ-$Al_{10-x}Cu_x$-SG) and its high efficiency in RWGS reaction. The combination of both EDTA and ED as structure directing agents is critical for integrating Cu species in the γ-Al_2O_3 lattice. The broad diffraction features and the absence of diffraction peaks of bulk CuO phase in mγ-$Al_{10-x}Cu_x$-SG catalysts indicates that the particle size of copper species is finely dispersed in the γ-Al_2O_3 lattice. The characteristic type IV isotherm and the pore size distribution with pore size in the range of 3–5 nm demonstrate the mγ-$Al_{10-x}Cu_x$-SG catalysts are mesoporous. The SEM-EDX analysis and FESEM EDX elemental mapping images of O, Al and Cu revealed that copper is well distributed in the alumina lattice, illustrating that homogenous hybridization of CuO species and alumina and hence an excellent interface interaction exists between copper and alumina in mγ-$Al_{10-x}Cu_x$-SG catalysts. The HRTEM analysis confirmed that the copper species in mγ-$Al_{10-x}Cu_x$-SG is nanocrystalline and there is a close contact between alumina and copper species through strong interaction of the Cu^{2+} ions with the γ-Al_2O_3 lattice. H_2-TPR analysis performed on mesoporous Al_9Cu_1 and the conventional γ-Al_9Cu_1-I catalysts provides further evidence on the strong copper-alumina (metal-support) interaction in mγ-$Al_{10-x}Cu_x$-SG catalysts. A detailed XPS analysis of mγ-$Al_{10-x}Cu_x$-SG catalysts and γ-Al_9Cu_1-I confirmed that Cu exists in +2 oxidation state in all catalysts. The detailed Cu—K edge EXAFS analysis of mγ-$Al_{10-x}Cu_x$-SG catalysts revealed that a long range structural order was lacking in mγ-$Al_{10-x}Cu_x$-SG catalysts likely due to the fine distribution of copper species in the alumina lattice and within the porous structure of the alumina leading to a strong copper (metal)-alumina (support) interaction.

The comparison of the catalytic activity between the mγ-$Al_{10-x}Cu_x$-SG catalysts and γ-Al_9Cu_1-I in RWGS reaction revealed that irrespective of the composition the mγ-$Al_{10-x}Cu_x$-SG catalysts showed high CO_2 conversion and catalytic stability than γ-Al_9Cu_1-I. For example, mesoporous Al_9Cu_1 displayed a CO_2 conversion of 45 % at 500 °C, which is about 2.8 times higher activity than γ-Al_9Cu_1-I catalyst with almost same Cu loading as that of Al_9Cu_1. Time-on-stream studies on mγ-$Al_{10-x}Cu_x$-SG catalysts at 500 °C over a period of 50 h revealed that the catalyst at low Cu loading (mγ-$Al_{9.9}Cu_{0.1}$) showed excellent catalytic stability, whereas the higher Cu loaded sample mγ-Al_9Cu_1 resulted only 5.9 % decrease in the activity. This result is highly promising when considering the poor thermal stability of Cu-based catalysts at ≥5 wt% Cu reported in the literature. A detailed structure-activity study revealed that in comparison with conventional γ-Al_9Cu_1-I catalyst the superior catalytic performance of mγ-$Al_{10-x}Cu_x$-SG catalysts is due to the fine distribution of Cu species in the alumina lattice, modified metal-alumina interface, enhanced charge transfer and electrochemical surface area, and the strong copper-alumina interaction as evidenced from XRD, SEM/TEM, TPR, electrochemical characterization, XPS and Cu K-edge XAS studies. The presence of mesopores and macropores in mγ-$Al_{10-x}Cu_x$-SG catalysts reduces the diffusion limitation of the reactants and products, avoid the pressure drop problem during catalysis and also offers a spatial confinement effect to the active CuO_x species. DFT studies revealed that the mechanism of CO_2 reduction to CO formation by RWGS reaction on mγ-$Al_{10-x}Cu_x$-SG catalysts is preceded through the formation of a hydroxycarbonyl (OCOH) intermediate. *The Operando* DRIFTS-MS analysis of RWGS over Al_9Cu_1 catalyst substantiate the DFT results and the proposed reaction mechanism that the reaction goes through a

redox mechanism with the formation of hydroxycarbonyl intermediates, which are rapidly decomposed into CO and H_2O. In this pathway, the redox pair $Cu^0/Cu^{\delta+}$ plays a key role. The activity and stability of mγ-$Al_{10-x}Cu_x$-SG catalysts can be further improved by introducing other electronically interacting and/or structurally modifying elements in it, the sol-gel synthesis strategy described in this work is highly promising for that.

CRediT authorship contribution statement

Simi Saju: Writing – original draft, Visualization, Validation, Investigation. **Sivaraj Rajendran:** Writing – original draft, Visualization, Validation, Investigation. **Ulviye Öztas:** Writing – original draft, Validation, Investigation. **Sergio Carrasco Ruiz:** Writing – original draft, Visualization, Validation, Investigation. **Tomas Ramirez Reina:** Writing – review & editing, Visualization, Validation, Investigation. **Biplab Ghosh:** Writing – original draft, Visualization, Validation, Investigation. **Sreeprasanth Pulinthanathu Sree:** Writing – original draft, Visualization, Validation, Investigation. **Raghavendra Meena:** Writing – original draft, Visualization, Validation, Investigation. **Guanna Li:** Writing – original draft, Visualization, Validation, Investigation. **Luis F. Bobadilla:** Investigation, Methodology. **Chathakudath P. Vinod:** Investigation. **Thomas Mathew:** Writing – review & editing, Supervision, Project administration, Methodology, Investigation. **N. Raveendran Shiju:** Writing – review & editing, Visualization, Supervision, Resources, Project administration, Funding acquisition, Conceptualization.

Declaration of competing interest

The authors declare that they have no known competing financial interests or personal relationships that could have appeared to influence the work reported in this paper.

Acknowledgment

TM and NRS thank Holland Research School of Molecular Chemistry (HRSMC) for granting an incoming fellowship to TM to work at the Catalysis Engineering Group, University of Amsterdam, The Netherlands. SS gratefully acknowledges Department of Science and Technology (DST), New Delhi, for the facility support under the DST-FIST program in St. John's College, Anchal, Kerala, India. SR thanks the University Grants Commission (UGC) for research fellowship. We acknowledge Harshini V. Annadata for EXAFS analysis and interpretations. We also acknowledge Beamline Development & Application Section, Bhabha Atomic Research Center, Mumbai for EXAFS measurements. We thank Dr. Joseph Jolly V. L, St. Thomas College, Thrissur, Kerala, India for XRD measurements. The DFT calculations were performed using the Dutch national e-infrastructure with the support of the SURF Cooperative using grant no. EINF-7987.

Appendix A. Supplementary data

Supplementary data to this article can be found online at https://doi.org/10.1016/j.cej.2025.169863.

Data availability

Data will be made available on request.

References

[1] M.D. Porosoff, B. Yan, J.G. Chen, Energ. Environ. Sci. 9 (2016) 62–73.
[2] T. Mathew, S. Saju, S.N. Raveendran, Eng. Solut. CO_2 Convers, John Wiley & Sons, Ltd, 2021, pp. 281–316;
E.D. Batyrev, N.R. Shiju, G. Rothenberg, J. Phys. Chem. C 116 (2012) 19335–19341.
[3] A. Rafiee, M. Panahi, K.R. Khalilpour, J. CO2 Util. 18 (2017) 98–106.
[4] Y.A. Daza, J.N. Kuhn, RSC Adv. 6 (2016) 49675–49691;
E.V. Ramos-Fernandez, N.R. Shiju, G. Rothenberg, RSC Adv. 4 (2014) 16456–16463.
[5] L. Yang, L. Pastor-Pérez, S. Gu, A. Sepúlveda-Escribano, T.R. Reina, Appl. Catal. Environ. 232 (2018) 464–471.
[6] X. Su, X. Yang, B. Zhao, Y. Huang, J. Energy Chem. 26 (2017) 854–867.
[7] J. Yu, X. Sun, X. Tong, J. Zhang, J. Li, S. Li, Y. Liu, N. Tsubaki, T. Abe, J. Sun, Nat. Commun. 12 (2021) 1–10.
[8] H.-X. Liu, S.-Q. Li, W.-W. Wang, W.-Z. Yu, W.-J. Zhang, C. Ma, C.-J. Jia, Nat. Commun. 13 (2022) 867.
[9] C. Álvarez Galván, J. Schumann, M. Behrens, J.L.G. Fierro, R. Schlögl, E. Frei, Appl. Catal. Environ. 195 (2016) 104–111.
[10] D. Vovchok, C. Zhang, S. Hwang, L. Jiao, F. Zhang, Z. Liu, S.D. Senanayake, J. A. Rodriguez, ACS Catal. 10 (2020) 10216–10228.
[11] L. Pastor-Pérez, F. Baibars, E. Le Sache, H. Arellano-García, S. Gu, T.R. Reina, J. CO2 Util. 21 (2017) 423–428.
[12] M. Ronda-Lloret, S. Rico-Francés, A. Sepúlveda-Escribano, E.V. Ramos-Fernandez, Appl. Catal. Gen. 562 (2018) 28–36.
[13] C.S. Chen, W.H. Cheng, S.S. Lin, Chem. Commun. 1 (2001) 1770–1771.
[14] J. Schumann, M. Eichelbaum, T. Lunkenbein, N. Thomas, M.C. Álvarez Galván, R. Schlögl, M. Behrens, ACS Catal. 5 (2015) 3260–3270.
[15] X. Zhang, X. Zhu, L. Lin, S. Yao, M. Zhang, X. Liu, X. Wang, Y.W. Li, C. Shi, D. Ma, ACS Catal. 7 (2017) 912–918.
[16] R. Jin, J. Easa, C.P. O'Brien, ACS Appl. Mater. Interfaces 13 (2021) 38213–38220.
[17] A.M. Bahmanpour, F. Héroguel, M. Kllıç, C.J. Baranowski, L. Artiglia, U. Röthlisberger, J.S. Luterbacher, O. Kröcher, ACS Catal. 9 (2019) 6243–6251.
[18] Y. Chen, H. Hong, J. Cai, Z. Li, ChemCatChem 13 (2021) 656–663.
[19] B. Lu, K. Kawamoto, Catal. Sci. Technol. 4 (2014) 4313–4321.
[20] Y. Choi, G.D. Sim, U. Jung, Y. Park, M.H. Youn, D.H. Chun, G.B. Rhim, K.Y. Kim, K. Y. Koo, Chem. Eng. J. 492 (2024) 152283.
[21] E. Lam, J.J. Corral-P'erez, K. Larmier, G. Noh, P. Wolf, A. Comas-Vives, A. Urakawa, C. Cop'eret, Angew. Chem. Int. Ed. 58 (2019) 13989–13996.
[22] X. Xu, S.K. Megarajan, Y. Zhang, H. Jiang, Chem. Mater. 32 (2020) 3–26.
[23] T. Mathew, K. Sivaranjani, E.S. Gnanakumar, Y. Yamada, T. Kobayashi, C. S. Gopinath, J. Mater. Chem. 22 (2012) 13484–13493.
[24] X. Ai, H. Xie, S. Chen, G. Zhang, B. Xu, G. Zhou, Int. J. Hydrogen Energy 47 (2022) 14884–14895.
[25] S. Rajendran, S.S. Mani, T.R. Nivedhitha, A.K. Asoka, P.S. Arun, T. Mathew, C. S. Gopinath, ACS Appl. Energy Mater. 7 (2024) 104–116.
[26] T. Mathew, Y. Yamada, A. Ueda, H. Shioyama, T. Kobayashi, Appl. Catal. Gen. 286 (2005) 11–22.
[27] A.K. Poswal, A. Agrawal, H.K. Poswal, D. Bhattacharyya, S.N. Jha, N.K. Sahoo, J. Synchrotron Radiat. 23 (2016) 1518–1525.
[28] B. Ravel, M. Newville, J. Synchrotron Radiat. 12 (2005) 537–541.
[29] G.G. Tunell, E. Posnjak, C.J. Ksanda, Zeitschrift Für Krist. - Cryst. Mater. 90 (1935) 120–142.
[30] M. Ronda-Lloret, L. Yang, M. Hammerton, V.S. Marakatti, M. Tromp, Z. Sofer, A. Sepúlveda-Escribano, E.V. Ramos-Fernandez, J.J. Delgado, G. Rothenberg, T. Ramirez Reina, N.R. Shiju, ACS Sustain. Chem. Eng. 9 (2021) 4957–4966;
M. Ronda-Lloret, V.S. Marakatti, W.G. Sloof, J.J. Delgado, A. Sepúlveda-Escribano, E.V. Ramos-Fernandez, G. Rothenberg, N.R. Shiju, ChemSusChem 13 (2020) 6401–6408.
[31] G. Kresse, J. Furthmüller, Comput. Mater. Sci. 6 (1996) 15–50.
[32] G. Kresse, J. Furthmüller, Phys. Rev. B 54 (1996) 11169–11186.
[33] J.P. Perdew, K. Burke, M. Ernzerhof, Phys. Rev. Lett. 77 (1996) 3865–3868.
[34] R. Tran, Z. Xu, B. Radhakrishnan, D. Winston, W. Sun, K.A. Persson, S.P. Ong, Sci Data 3 (2016) 160080.
[35] L. Shi, Y. Huang, Z.-H. Lu, W. Cen, X. Yu, S. Qing, Z. Gao, R. Zhang, G. Feng, Appl. Surf. Sci. 535 (2021) 147651.
[36] X. Krokidis, P. Raybaud, A.-E. Gobichon, B. Rebours, P. Euzen, H. Toulhoat, J. Phys. Chem. B 105 (22) (2001) 5121–5130.
[37] S. Grimme, J. Antony, S. Ehrlich, H. Krieg, J. Chem. Phys. 132 (2010) 154104.
[38] S. Grimme, S. Ehrlich, L. Goerigk, J. Comput. Chem. 32 (2011) 1456–1465.
[39] V. Wang, N. Xu, J.-C. Liu, G. Tang, W.-T. Geng, Comput. Phys. Commun. 267 (2021) 108033.
[40] L. Dimesso, Handb. Sol-Gel Sci. Technol. Process. Charact. Appl. (2018) 1067–1087.
[41] A. Kubiak, Z. Bielan, M. Kubacka, E. Gabała, A. Zgoła-Grześkowiak, M. Janczarek, M. Zalas, A. Zielińska-Jurek, K. Siwińska-Ciesielczyk, T. Jesionowski, Appl. Surf. Sci. 520 (2020) 146344.
[42] B. Bridier, N. López, J. Pérez-Ramírez, J. Catal. 269 (2010) 80–92.
[43] T. Mathew, N.R. Shiju, K. Sreekumar, B.S. Rao, C.S. Gopinath, J. Catal. 210 (2002) 405–417.
[44] L.K. Preethi, R.P. Antony, T. Mathews, L. Walczak, C.S. Gopinath, Sci. Rep. 7 (2017) 14314.
[45] W.-P. Dow, T.-J. Huang, J. Catal. 160 (1996) 171–182.
[46] S. Velu, K. Suzuki, C.S. Gopinath, H. Yoshida, T. Hattori, Phys. Chem. Chem. Phys. 4 (2002) 1990–1999.
[47] K. Roy, C.P. Vinod, C.S. Gopinath, J. Phys. Chem. C 117 (2013) 4717–4726.
[48] J.E. Castle, Surf. Interface Anal. 6 (1984) 302.
[49] X. Liu, S. Cui, Z. Sun, Y. Ren, X. Zhang, P. Du, J. Phys. Chem. C 120 (2016) 831–840.
[50] N. Kanjanasoontorn, T. Permsirivanich, T. Numpilai, T. Witoon, N. Chanlek, M. Niamlaem, C. Warakulwit, J. Limtrakul, Catal. Letters 146 (2016) 1943–1955.

[51] I.A. Hassan, S. Sathasivam, H.U. Islam, S.P. Nair, C.J. Carmalt, RSC Adv. 7 (2017) 551–558.
[52] M.C. Hsiao, H.P. Wang, Y.W. Yang, Environ. Sci. Technol. 35 (2001) 2532–2535.
[53] D. Vovchok, J. Tata, I. Orozco, F. Zhang, R.M. Palomino, W. Xu, L. Harper, S. J. Khatib, J.A. Rodriguez, S.D. Senanayake, Catal. Today 323 (2019) 216–224.
[54] B. Lv, J. Yu, F. Zhou, Z. Wang, J. Zhang, Y. Zhang, Y. Wu, Y. Wang, W. Luo, Mol. Catal. 578 (2025) 114978.
[55] S.S. Mani, S. Rajendran, N. Nalajala, T. Mathew, C.S. Gopinath, Energ. Technol. 10 (2022) 2100356.
[56] K. Roy, C.S. Gopinath, Anal. Chem. 86 (2014) 3683–3687.
[57] G. Busca, V. Lorenzelli, Mater. Chem. 7 (1982) 89–126.
[58] O. Cheung, Q. Liu, Z. Bacsik, N. Hedin, Microporous Mesoporous Mater. 156 (2012) 90–96.
[59] G. Busca, Catal. Today 226 (2014) 2–13.
[60] Libor Kovarik, Mark Bowden, János Szanyi, J. Catal. 393 (2021) 357–368.
[61] X. Song, C. Yang, X. Li, Z. Wang, C. Pei, Z.-J. Zhao, J. Gong, ACS Catal. 12 (2022) 14162–14172.
[62] J. Baltrusaitis, J.H. Jensen, V.H. Grassian, J. Phys. Chem. B 110 (24) (2006) 12005–12016.
[63] H. Zhang, P. Han, D. Wu, C. Du, J. Zhao, K.H.L. Zhang, J. Lin, S. Wan, J. Huang, S. Wang, H. Xiong, Y. Wang, Nat. Commun. 14 (1) (2023) 7705.
[64] D. Álvarez-Hernández, M. Marín-Sánchez, L. Lobo-Andrades, L. Azancot, L. F. Bobadilla, S. Ivanova, M.A. Centeno, Catal. Today 422 (2023) 114235.
[65] S. Jiang, L. D'Amario, H. Dau, ChemSusChem 15 (8) (2022) e202102506.
[66] N.T.T. Ha, V.T.M. Hue, B.C. Trinh, N.N. Ha, L.M. Cam, J. Chem. (2019) 4341056, https://doi.org/10.1155/2019/4341056.
[67] L.F. Bobadilla, J.L. Santos, S. Ivanova, J.A. Odriozola, A. Urakawa, ACS Catal. 8 (2018) 7455–7467.
[68] J.A. Rodríguez, J. Evans, J. Graciani, J.-B. Park, P. Liu, J. Hrbek, J.F. Sanz, J. Phys. Chem. C 113 (2009) 7364–7370.
[69] J.A. Rodriguez, P. Liu, D.J. Stacchiola, S.D. Senanayake, M.G. White, J.G. Chen, ACS Catal. 5 (2015) 6696–6706.